

Supplementary information

Inter-facet junction effects on particulate photoelectrodes

In the format provided by the authors and unedited

Supplementary Information

Inter-facet junction effects on particulate photoelectrodes

Xianwen Mao and Peng Chen*

*Correspondence to: pc252@cornell.edu

Table of Contents

1	Data acquisition and analysis of multimodal photoelectrode performance metric imaging	3
1.1	Determination of the spatial resolution in subfacet photocurrent mapping.....	3
1.2	Quantification of subfacet-level photocurrents.....	4
1.3	Analysis of potential dependences of subfacet-level photocurrents to extract local photoelectrochemical property parameters V_{FB} and η_{sep}	4
1.4	Quantitative single-molecule localization and counting for charge carrier reaction imaging	6
1.5	Correlating SEM structural contours with optical microscopy images to pinpoint the on-particle locations in subfacet photocurrent mapping and charge carrier reaction imaging	8
1.6	Particle dissection to probe subfacet spatial variations of charge carrier activities	8
1.7	Analysis of potential dependences of charge carrier reaction rates on dissected segments to extract local photoelectrochemical property parameters V_{FB} , k_h and k_e	9
1.8	Light attenuation correction for subfacet-level photocurrents and carrier reaction rates on the {110} facet	11
1.9	Calculation of experimentally measured single-whole-particle photocurrent density	11
2	Control experiments and additional discussions/analyses	12
2.1	Energy-level analysis shows that the photogenerated holes and electrons in BiVO_4 can thermodynamically oxidize the hole-probe (amplex red) and reduce the electron-probe (resazurin), respectively.....	12
2.2	Ensemble results and ensemble-averaged single-particle results show that BiVO_4 can photoelectrocatalytically oxidize the hole-probe and reduce the electron-probe to generate the product molecule resorufin, and the rates of hole/electron probe reactions are negligible under the dark condition (i.e., without 405-nm illumination to generate charge carriers in BiVO_4)....	13
2.3	The hole and electron probe reactant molecules adsorb to all surface sites equivalently on the entire catalyst particle (i.e., no preferential adsorptions on certain facets, edges, corners or other subparticle regions).....	13
2.4	In our charge carrier reaction imaging, illumination is spatially uniform and reaction products have spatially uniform fluorescence intensities, and thus there is no spatially biased detection.....	14
2.5	For inter-facet edges with no inter-facet junction effect (i.e., edge formed between two identical {110} facets), there is no micrometer-sized spatial variation of hole/electron probe reaction rates	15
2.6	Modelling the facet size (i.e., $L_{\{010\}}$ and $L_{\{110\}}$) scaling laws of V_{FB} and η_{sep} at the {010} {110} inter-facet edge and intrinsic to the two facets	16
2.7	Quantitative prediction of decoupled, two-dimensional facet size (i.e., $L_{\{010\}}$ and $L_{\{110\}}$) dependences of single-whole-particle photocurrent densities	17
2.8	Quantitative prediction of decoupled, two-dimensional facet size (i.e., $L_{\{010\}}$ and $L_{\{110\}}$) dependences of j_{ph} -vs.- V behavior and optimal operating condition of a whole particle	18
2.9	Determination of the surface dopant densities on the {010} and {110} facets based on experimentally measured V_{FB} spatial profiles across inter-facet junctions	19
2.10	Calculation of the facet-specific near-edge surface transition zone width (i.e., $W_{\{010\}}$ and $W_{\{110\}}$) dependences of $L_{\{110\}}^{level-off}$	19
2.11	Analysis and discussion of the single molecule fluorescence imaging results on N_2 -treated BiVO_4 particles	20
2.12	Stability of N_2 -treated BiVO_4 particles under operating conditions	20
2.13	Effects of nitrogen doping on the electronic and photoelectrochemical properties of BiVO_4	21
2.14	Discussion of the effects of cocatalysts and future research opportunities	22
3	Additional data and figures	23
4	Additional references	37

1 Data acquisition and analysis of multimodal photoelectrode performance metric imaging

1.1 Determination of the spatial resolution in subfacet photocurrent mapping

The spatial resolution in our subfacet photocurrent mapping is determined by the 405-nm laser focus size. The 405-nm laser was focused on a bare ITO electrode and a reflection image (Fig. S1a) was captured by the EMCCD camera. This image was then fitted with a 2D Gaussian function to determine the focused laser spot size (Eq. S1):

$$I(x, y) = A \exp \left[-\frac{(x - x_{0,\text{laser}})^2}{2\sigma_{x,\text{laser}}^2} - \frac{(y - y_{0,\text{laser}})^2}{2\sigma_{y,\text{laser}}^2} \right] + B \quad \text{Eq. S1}$$

where $I(x, y)$ is the laser intensity at the (x, y) position, and A , B , $(x_{0,\text{laser}}, y_{0,\text{laser}})$ and $(\sigma_{x,\text{laser}}, \sigma_{y,\text{laser}})$ are the amplitude, background, centroid and standard deviation along the x - or y -coordinate of the 2D Gaussian function. The laser spot size was taken as the full-width-at-half-maximum (FWHM) of this Gaussian function, which is about 382 nm (Fig. S1b). The {010} and {110} facets of a single BiVO₄ particle is clearly visible in the optical transmission image (Fig. S1c) and by moving the microscope sample stage, the focused 405-nm laser (the exact location of which is registered by the centroid of the Gaussian function Eq. S1) can be placed at any subfacet location within a particle (Fig. S1d).

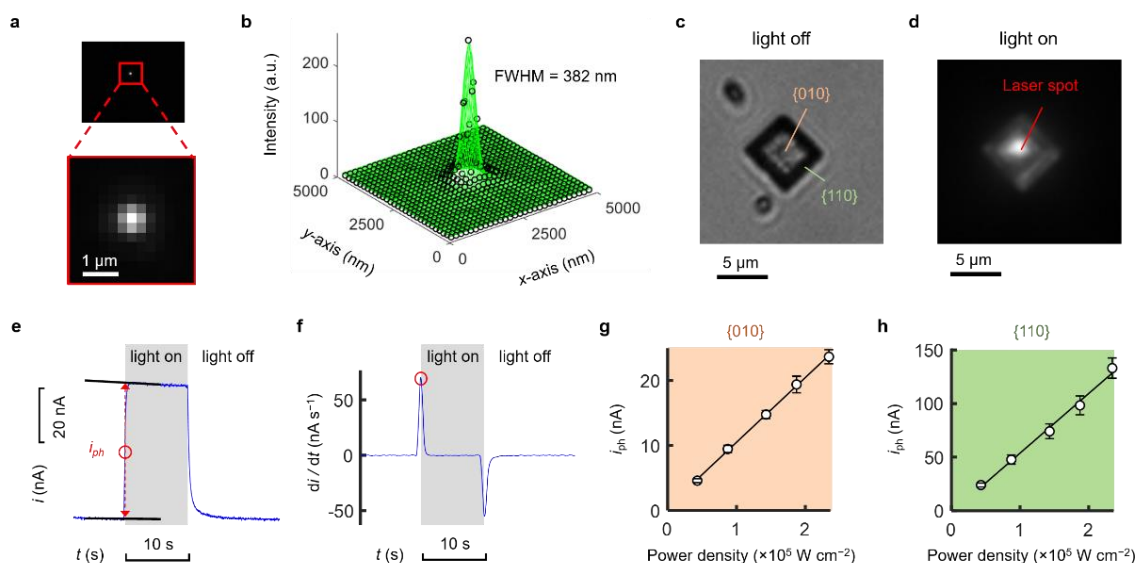


Fig. S1. Measurement of subfacet-level photocurrents. (a) Reflection image of a focused 405-nm laser on a bare ITO electrode. (b) 2D Gaussian fitting (Eq. S1) of the laser intensity profile of the red box in a. The laser spot size was taken as the full-width-at-half-maximum (FWHM) of the Gaussian function, which is ~382 nm. (c) Transmission image of a single BiVO₄ particle when the 405-nm laser is off. The {010} and {110} facets are distinguishable. (d) Transmission image of the particle in c when it is illuminated with a focused 405-nm laser. (e) Representative current – time ($i - t$) response (i.e., chronoamperometric trajectory) recorded by a potentiostat when a focused 405 nm laser excites a subfacet location on a single BiVO₄ particle. The light-on period is 10 s and the light-off period is 15 s. The photocurrent (i_{ph}) is determined by the current enhancement (red double arrow) when the illumination is turned on; the exact time of this steep increase in current (red circle) is determined by the maximum in the corresponding di/dt trajectory in f. For details on photocurrent determination, see section 1.2. (f) Calculated $di/dt - t$ trajectory for the $i - t$ response in e, showing that the exact time where a sharp increase in current occurs is determined by the maximum in the corresponding di/dt trajectory. (g, h) Representative subfacet-level photocurrents obtained at 1.03 V versus 405-nm laser power density obtained on the {010} facet (g) and on the {110} facet (h) of a single BiVO₄ particle, showing a linear relationship between the photocurrent and the laser power density. Solid line: linear fit. Error bar: s.d.

1.2 Quantification of subfacet-level photocurrents

After a focused 405-nm laser spot was placed at a selected subfacet location, chronoamperometric measurements at a selected potential were performed during light-chopping (typically the on-period is 10 s and the off-period is 15 s, and the number of on-off cycles is 10), and the resulting current – time ($i - t$) response (Fig. S1e) was recorded. When the illumination is turned on, a clear current enhancement can be observed when an anodic potential is applied (*e.g.*, 1.13 V) and appreciable anodic photocurrent associated with water oxidation is present. Next, the first derivative of the $i - t$ response (*i.e.*, $di/dt - t$ trajectory; Fig. S1f) was calculated and the time corresponding to the local maximum in di/dt within a light on/off cycle was registered as the time of turning illumination on (t_{on}) (red circle in Fig. S1f). To quantify the photocurrent, the currents for the two 3 s durations on either side of the time of turning illumination on, ($t_{on} - 4$ s, $t_{on} - 1$ s) and ($t_{on} + 1$ s, $t_{on} + 4$ s) were fitted with two different linear functions (black lines in Fig. S1e), the difference in these two linear functions at t_{on} (red double arrow in Fig. S1e) was taken as the photocurrent (*i.e.*, i_{ph}) for this light on/off cycle. The i_{ph} value averaged over several light on/off cycles was reported as the photocurrent at a particular applied potential associated with a specific subfacet location. Representative subfacet-level photocurrents *versus* 405-nm laser power densities obtained on the {010} facet (Fig. S1g) and on the {110} facet (Fig. S1h) of a single BiVO₄ particle show a linear relationship between the photocurrent and the power density.

1.3 Analysis of potential dependences of subfacet-level photocurrents to extract local photoelectrochemical property parameters V_{FB} and η_{sep}

The photocurrent (i_{ph}) - applied potential (V) relationship was fitted using a modified Reichmann model^{1,2} (Eq. S2 - Eq. S13) for the minority carrier (hole) photocurrent of n -type semiconductor at the semiconductor/electrolyte interface. The i_{ph} expression is given by:

$$i_{ph} = j_{pc} \left[\left(\frac{-C + (C^2 + 4AB)^{1/2}}{2A} \right)^2 - 1 \right] \times \eta_{sep} \times S \quad \text{Eq. S2}$$

$$A = j_{pc} + j_s e^{-\frac{V_a}{V_{th}}} \quad \text{Eq. S3}$$

$$B = j_{pc} + j_G \quad \text{Eq. S4}$$

$$C = \frac{qV_{th}n_i w e^{-\frac{V_a}{2V_{th}}}}{4t_h V_{sc}} \quad \text{Eq. S5}$$

where j_{pc} is the hole exchange current density, j_s is the saturation current density, j_G is the Gartner's expression of photocurrent density³, η_{sep} is the absorbed photon to current efficiency (*i.e.*, the efficiency of charge separation in the depletion zone and transport to the collecting contact), S is the illumination area, V_a is the voltage applied to the semiconductor with respect to the equilibrium unbiased situation in the dark, V_{th} is the thermal voltage, q is the elementary charge, n_i is the intrinsic carrier concentration in the bulk of the semiconductor, w is the width of the space-charge region in the semiconductor at the SEI, t_h is the minority carrier lifetime, and V_{sc} is the potential drop in the space-charge region in the semiconductor at the SEI.

The hole exchange current density j_{pc} is calculated by

$$j_{\text{pc}} = qk_{\text{tr}}p_{\text{dark},0} \quad \text{Eq. S6}$$

where k_{tr} is the rate constant for charge transfer of valence-band hole to the electrolyte, and $p_{\text{dark},0}$ is the interfacial hole concentration (i.e., the hole concentration at the SEI) in the dark. $p_{\text{dark},0}$ is calculated by

$$p_{\text{dark},0} = \frac{n_i^2}{N_{\text{D}}} \exp\left(\frac{\text{sign}(V_{\text{sc}}) \frac{qN_{\text{D}}}{2\varepsilon_0\varepsilon_r} w^2}{V_{\text{th}}}\right) \quad \text{Eq. S7}$$

where N_{D} is the donor concentration in the bulk of the semiconductor, ε_0 is the vacuum permittivity, and ε_r is the relative permittivity. The saturation current density, j_s , is given by

$$j_s = \frac{qn_i^2L_{\text{h}}}{t_{\text{h}}N_{\text{D}}} \quad \text{Eq. S8}$$

where L_{h} is the hole diffusion length. The Gartner's expression of photocurrent density³, j_{G} , is given by

$$j_{\text{G}} = qP \left(1 - \frac{e^{-\alpha w}}{1 + \alpha L_{\text{h}}}\right) \quad \text{Eq. S9}$$

where P is the incident power density, and α is the absorption coefficient. The potential drop in the space-charge region in the semiconductor at the SEI, V_{sc} , is given by

$$V_{\text{sc}} = V - V_{\text{FB}} \quad \text{Eq. S10}$$

where V_{FB} is the flat band potential of the semiconductor referenced to RHE. The voltage of the semiconductor with respect to the equilibrium unbiased situation in the dark, V_{a} , is calculated by

$$V_{\text{a}} = V_{\text{sc}} - V_{\text{bi}} \quad \text{Eq. S11}$$

where V_{bi} is the built-in potential of the semiconductor/electrolyte junction. The intrinsic carrier concentration, n_i , is given by

$$n_i = \sqrt{N_{\text{C}}N_{\text{V}} \exp\left(-\frac{E_{\text{g}}}{k_{\text{B}}T}\right)} \quad \text{Eq. S12}$$

where N_{C} is the effective density of states of the conduction band, N_{V} is the effective density of state of the valence band, E_{g} is the band-gap energy, k_{B} is the Boltzmann constant, and T is the absolute temperature. The width of the space-charge region in the semiconductor at the SEI, w , is given by

$$w = \sqrt{\frac{2\varepsilon_0\varepsilon_r}{qN_D}V_{sc}} \quad \text{Eq. S13}$$

The values of physical constants and material parameters of BiVO₄ used in the calculations are listed in Table S1. The modified Reichmann model (Eq. S2 - Eq. S13) contains only two unknown fitting parameters, η_{sep} and V_{FB} . Fitting $j_{ph} - V$ data obtained at a subfacet location yields the local η_{sep} and V_{FB} .

Table S1. Values of physical constants and material parameters of BiVO₄ used in the calculations

Description	Value
Boltzmann constant (k_B)	$8.6 \times 10^{-5} \text{ eV K}^{-1}$
elementary charge (q)	$1.6 \times 10^{-19} \text{ C}$
thermal voltage (V_{th})	25.9 mV
vacuum permittivity (ε_0)	$8.85 \times 10^{-12} \text{ F m}^{-1}$
donor concentration (N_D)	$1 \times 10^{18} \text{ cm}^{-3}$ ⁴
relative permittivity (ε_r)	68 ⁴
effective density of states of conduction band (N_C)	$2.3 \times 10^{19} \text{ cm}^{-3}$ ⁵
effective density of states of valence band (N_V)	$1.8 \times 10^{19} \text{ cm}^{-3}$ ⁵
bandgap energy (E_g)	2.4 eV ⁶
Hole (minority carrier) lifetime (t_h)	40 ns ⁷
hole diffusion length (L_h)	70 nm ⁷
rate constant for hole transfer to electrolyte (k_{tr})	$1.4 \times 10^{-6} \text{ cm s}^{-1}$ ^{a 8}
electron mobility (μ_n)	$4 \times 10^{-2} \text{ cm}^2 \text{ V}^{-1} \text{ s}^{-1}$ ⁷
majority carrier collection velocity (v_c)	$1 \times 10^2 \text{ cm s}^{-1}$ ^{b 4,9-11}
absorption coefficient at 405 nm (α)	$3.7 \times 10^4 \text{ cm}^{-1}$ ⁴

Notes: (a) Determined by bulk BiVO₄ measurements (Fig. S10g)⁸; (b) Estimated by SEI depletion width / photoexcited carrier recombination lifetime in BiVO₄^{4,9-11}.

1.4 Quantitative single-molecule localization and counting for charge carrier reaction imaging

The fluorescence movies obtained in the presence of hole-probe (i.e., amplex red) or electron-probe (i.e., resazurin) for quantitative charge carrier reaction imaging were analyzed using a home-written MATLAB program that integrates iQPALM (image-based quantitative photo-activated localization microscopy) and a quantitative single-molecule counting algorithm; the full details of these data analysis procedures are described in our previous work¹²⁻¹⁵. A brief summary of such data analysis is provided here. The microscope stage drift was monitored in a frame-by-frame fashion by calculating the intensity-weighted centroid position of the stable intrinsic photoluminescence of the BiVO₄ particle. The average drift of multiple particles present in the same movie was used to correct the centroid position of each candidate fluorescent product molecule. Because the BiVO₄ particles are constantly bright objects, prior to extraction of single-molecule fluorescence signals from the images, the average photoluminescence of the BiVO₄ crystals was subtracted. 1000 frames in the absence of the fluorogenic reactant (i.e., hole-probe amplex red or electron-probe resazurin) were recorded and averaged to generate the average photoluminescence image. Each frame in the catalysis experiment in the presence of fluorogenic reactant was subtracted by the stage-drift-corrected, averaged photoluminescence image. Before the subtraction of the BiVO₄ photoluminescence, images to be subtracted are expanded by 10 times in x and y dimensions to accommodate corrections that are subpixel-level stage drifts and, after subtraction, the expanded images are re-binned to the original image size (i.e., decreasing the image size by 10 times in both x and y dimensions). After the subtraction of the BiVO₄ photoluminescence, the pixels with an intensity value larger than the mean pixel intensity plus six standard deviations were identified as *potential* single molecule

fluorescence signals. Next, a 13×13 pixel² area (each pixel is ~ 267 nm) centered at each selected pixel was fitted with a two-dimensional Gaussian point spread function (PSF) to determine the centroid position (x_0, y_0) of each fluorescent product molecule. Such fitting also yields the standard deviation (σ_x, σ_y) and the integrated intensity of the PSF, as well as the localization error (Err_x, Err_y) of the centroid position. To remove noise contributions and spurious detections, and correct for unresolved multiple-molecule detections and over-counting due to a product molecule adsorbed on the particle for multiple frames, the selected and PSF-fitted candidate events (i.e., potential single-molecule fluorescence signals) were filtered by a quantitative single-molecule counting algorithm. Briefly, first, candidate events with their PSF σ_x or $\sigma_y < 100$ nm are rejected because these are representative of “hot” pixels since their PSF are too narrow for a single-molecule event (the ideal, theoretical σ_x, σ_y of the diffraction-limited PSF of a resorufin product molecule is ~ 126 nm)¹². Next, candidate events with their PSF width greater than 100 nm and less than a filter threshold value (σ_{filter} , usually ~ 220 nm; Fig. S2 a and b) are selected as single-molecule events. These single-molecule events are used to create super-resolution charge carrier reaction images (e.g., main text Fig. 1 e and f; Fig. S14). For those candidate events with their PSF σ_x or σ_y greater than σ_{filter} (e.g., Fig. S2 h-j where a significant population of the candidate events show broad σ_x distribution), if their PSF intensity is greater than the PSF intensity of a single-molecule event (see Fig. S2c), we choose them as multiple-molecule events with the number of molecules (rounded integers) determined by the total PSF intensity divided by the PSF intensity of a single-molecule event; otherwise they are rejected as a molecule that diffused significantly on the particle surface (about 5% of the observed events). The calculated specific reaction rate includes single-molecule and multiple-molecule events. Additionally, if two molecules are detected in two consecutive frames and the distance between their centroid locations in these two frames is less than 100 nm (about $2 \times \sqrt{Err_x^2 + Err_y^2}$, see Fig. S2 d and e), these two molecules are only counted once and the centroid position of the first of the two frames is recorded, in order to avoid the overestimation of catalytic activity due to multi-frame events (about 1% of the observed events) (i.e., product molecules adsorbed on catalysts for a time longer than a single frame acquisition time).

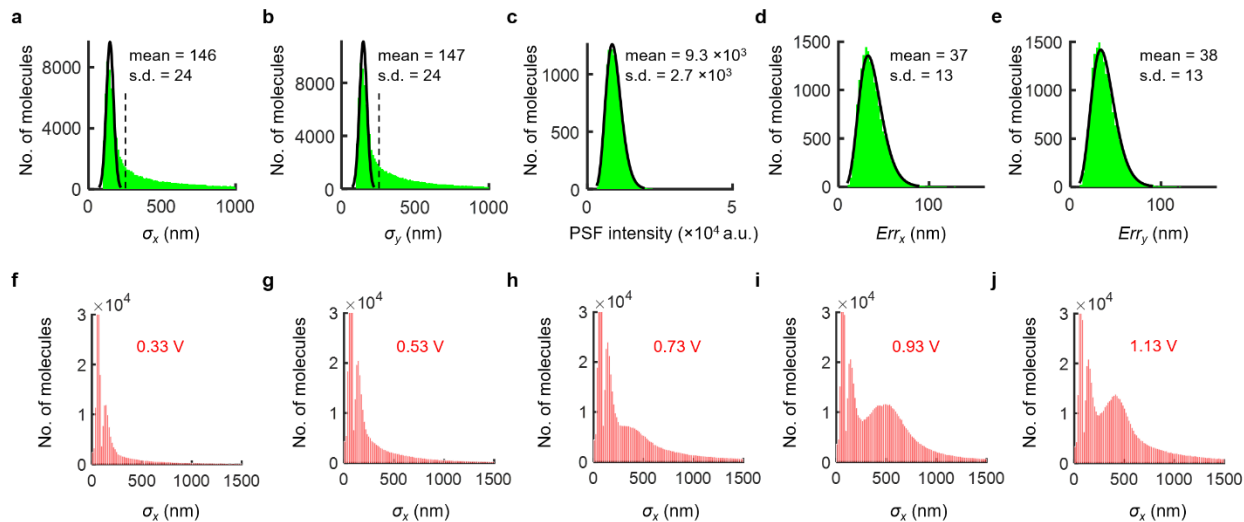


Fig. S2. Data analysis procedure for quantitative single molecule localization and counting using representative data on photoelectrocatalytic hole-probe oxidation as an example. (a, b) Distributions of σ_x (a) and σ_y (b) obtained with a representative fluorescence movie on photoelectrocatalytic oxidation of hole-probe amplex red (50 nM) on BiVO₄ at a potential of 0.33 V, a condition wherein the majority of the candidate events are single-molecule events. Hot-pixel events with $\sigma_x < 100$ nm or $\sigma_y < 100$ nm were removed here to show clearly the distributions. Black line: fit with a Gaussian distribution for data between 100 and 200 nm. σ_{filter} is defined as the smaller value of the mean of σ_x and σ_y data between 100 and 200 nm plus three standard deviations of this Gaussian fit (i.e., dashed vertical line in a and b). (c) Distribution of the PSF intensity of selected events that represent only single-molecule events (i.e., events with σ_x and σ_y between 100 and 200 nm) corresponding to the data and condition in a and b. Black line: fit with a Gamma distribution. (d, e) Distributions of Err_x (d) and Err_y (e) of selected events that represent only single-

molecule events (i.e., events with σ_x and σ_y between 100 and 200 nm) corresponding to the data and condition in a and b. Black line: fit with a Gamma distribution. (f-j) Distributions of unfiltered σ_x obtained at a series of applied potentials: 0.33 V (f), 0.53 V (g), 0.73 V (h), 0.93 V (i), and 1.13 V (j). Data in a is part of data in f.

1.5 Correlating SEM structural contours with optical microscopy images to pinpoint the on-particle locations in subfacet photocurrent mapping and charge carrier reaction imaging

The positions of the focused 405-nm laser beam in subfacet photocurrent mapping (Fig. S6, mode I) and the positions of the super-localized single molecule events in charge carrier reaction imaging (Fig. S6, mode II) are registered by spatial coordinates in optical microscopic (OM) images (either transmission image or fluorescence image; both have identical spatial coordinates). The structural contours of BiVO₄ particles (e.g., main text Fig. 1 e and f, Fig. S14), which can only be determined by SEM, need to be overlaid onto OM images in order to pinpoint the on-particle locations of either the focused laser or the single molecule events. Our multimodal photoelectrode performance metric imaging experiments were performed in regions with easily identifiable objects in both SEM and OM images, which enabled a straightforward correlation between the OM and SEM images. The SEM-OM overlay procedure for BiVO₄ particles with truncated bipyramid morphology is described in full detail in our earlier work¹³, and is briefly summarized here. For any BiVO₄ particle with a well-defined truncated bipyramidal morphology, its rectangular shape is visible in both the SEM and OM images, enabling establishing the correspondence between the vertices of the SEM rectangular structural contour and the vertices of the OM rectangular structural contour. Briefly, we determine the center position and orientation of each individual BiVO₄ particle from OM and SEM images by fitting its structure contour with a rectangle, and then perform the overlaying procedure based on the OM- and SEM-determined center positions and orientations. The overlay procedure for each individual BiVO₄ particle is based upon establishing a transformation relation from the OM image to the SEM image. Such transformation involves both translational and rotational moves. Therefore, the overall overlay error is associated with the translational error and the rotational error, and is generally about 5 to 10 nm¹³ due to this highly localized overlay procedure (i.e., correlating OM- and SEM-determined center positions and orientations of only a single particle of interest), which is significantly smaller than our single-molecule localization error (~ 40 nm; Fig. S2 d and e).

1.6 Particle dissection to probe subfacet spatial variations of charge carrier activities

The {010} and {110} facets of all the BiVO₄ particle measured in charge carrier reaction imaging are dissected into many segments (i.e., square-like thin strips; for example, the orange and green regions in Fig. S3 a and b), in order to quantify the specific hole/electron-probe reaction rates associated with a specific subfacet location (e.g., x_1 and x_2 in Fig. S3 a and b) and thus probe subfacet-level spatial variations of charge carrier reaction rates (Fig. S13, d and g) and, as a result, important local electronic properties (i.e., V_{FB} , k_e , k_h) (e.g., main text Fig. 1 i and j). First, based on the structural contours of a particle with a truncated bipyramid morphology determined by SEM (black lines in Fig. S3 b), we can determine the side lengths of the inner and outer squares (S_{inner} and S_{outer} ; Fig. S3 b), and thus quantify the sizes of the {010} and {110} facets ($L_{\{010\}}$ and $L_{\{110\}}$; Fig. S3 a) by the relations:

$$L_{\{010\}} = \frac{S_{inner}}{2} \quad \text{Eq. S14}$$

$$L_{\{110\}} = \frac{\sqrt{2}(S_{outer} - S_{inner})}{2} \quad \text{Eq. S15}$$

Next, the number of dissected segments to be generated on the {110} facet is chosen so as to ascertain the width of each strip-like segment ($b_{\{110\}}$; Fig. S3b) on the projected view to be about our single-molecule

localization error (~ 40 nm; Fig. S2 d and e). That is, the number of dissected segments on the $\{110\}$ is the round number of $L_{\{110\}} / (\sqrt{2} \times 40)$ nm (note that the $\sqrt{2}$ factor is to convert the $L_{\{110\}}$ value to that on the projected view). A similar dissection procedure was used for the $\{010\}$ facet to ascertain that the width of the outmost segment ($b_{\{010\}}$; Fig. S3b) is close to 40 nm; for inner segments where the number of detected product molecules decrease (due to smaller segment areas), we use larger segment widths (usually 2-fold or 3-fold increase). Fig. S3c illustrates how the dissected segments on the $\{010\}$ and $\{110\}$ facets of a particle relate to its inter-facet junction. The values of $\sqrt{2}b_{\{010\}}$ and $b_{\{110\}}$ are reported as the error bar for each subfacet location (also see main text Fig. 1h; Fig. S13, d and g). The center position of each dissected segment (e.g., x_1 and x_2 , Fig. S3 a and b) are reported as the subfacet location (also main text Fig. 1h; Fig. S13, d and g).

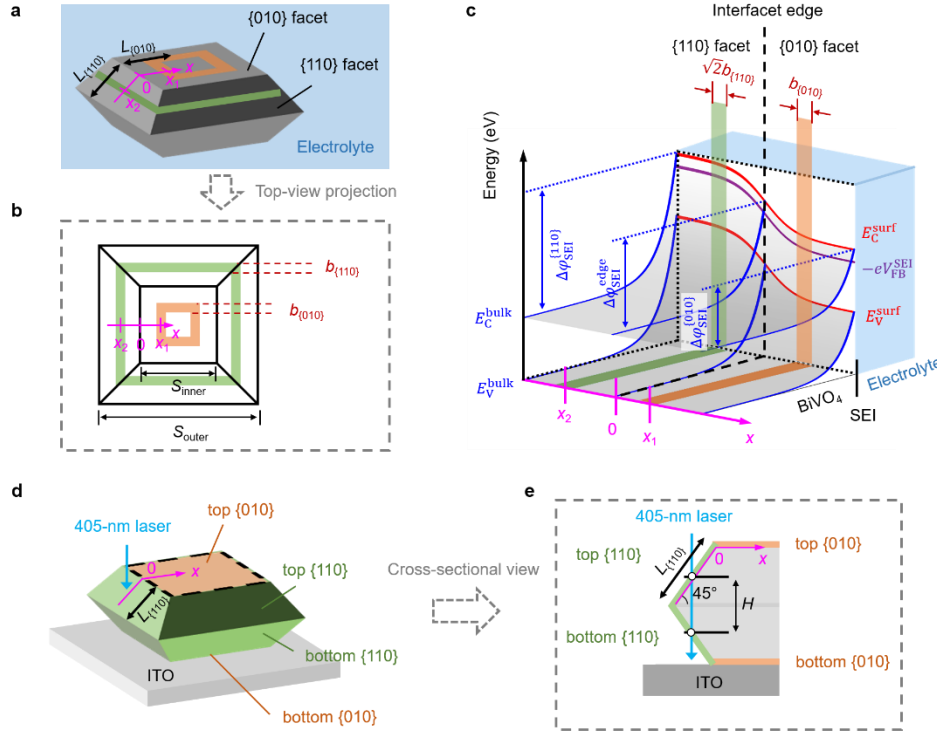


Fig. S3. Particle dissection and light attenuation correction. (a, b) Procedure of dissecting the $\{010\}$ and $\{110\}$ facets of a BiVO_4 particle into segments (i.e. thin strips, indicated by orange or green color for locations on the $\{010\}$ or $\{110\}$ facet, respectively) to quantify charge carrier activities at a subfacet location on the $\{010\}$ facet, x_1 , and another subfacet location on the $\{010\}$ facet, x_2 , in a 3D view of the particle surrounded by electrolyte solution (a) and in a top-view projection of the particle (b). (c) Schematic illustration of how the locations and widths of dissected segments on the $\{010\}$ and $\{110\}$ facets of a particle (i.e., x_1 , x_2 , $b_{\{010\}}$, $b_{\{110\}}$) relate to its inter-facet junction. (d, e) Schematic illustration of the 405-nm laser illumination configuration and the geometry of a BiVO_4 particle in our multimodal photoelectrode performance metric imaging experiments (Fig. S6) in a 3D view of the particle (d) and a cross-sectional view (e).

1.7 Analysis of potential dependences of charge carrier reaction rates on dissected segments to extract local photoelectrochemical property parameters V_{FB} , k_h and k_e

The $v_h - V$ relationship was fitted using a kinetic model developed previously¹⁶ that relates the reaction rate of the hole probe reaction (v_h) to the surface hole flux (F_h) by

$$v_h = k_h \sqrt{F_h} \quad \text{Eq. S16}$$

where k_h is the effective rate constant that reflects the surface hole activity, and has a unit of $s^{-1/2} m^{-1}$; note k_h depends on the hole-probe concentration in the solution, which is kept at 50 nM. The V dependence of F_h is given by the Reichmann's expression for minority carrier surface flux:

$$F_h = j_{pc} \left[\left(\frac{-C + (C^2 + 4AB)^{1/2}}{2A} \right)^2 - 1 \right] / q \quad \text{Eq. S17}$$

where A , B , C and j_{pc} are given in Eq. S3, Eq. S4, Eq. S5, and Eq. S6, respectively. This kinetic model is derived based on the mechanism that the reactant molecule of the hole probe reaction (i.e., amplex red) reacts with surface adsorbed hydroxyl radicals, which are produced by photogenerated holes reacting with adsorbed water molecules on the semiconductor^{16,17}. This mechanism is consistent with several previous studies¹⁸⁻²⁰ showing that amplex red molecules react with hydroxyl radicals. The kinetic model above (Eq. S16 and Eq. S17) contains two fitting parameters, k_h and V_{FB} . k_h reflects the intrinsic surface hole activity of the semiconductor material independent of light intensity and applied potential. Since the derivation of Eq. S16 and Eq. S17 assumes that the electron-hole separation efficiency is unity for the surface hole flux, which is not true for real semiconductor material systems, k_h contains contribution from the actual charge separation efficiency (i.e., η_{sep}). As more efficient electron-hole separation would result in a larger surface hole flux, a material system with a higher η_{sep} value would be manifested by a larger k_h value.

The $v_e - V$ relationship was fitted using a kinetic model developed previously¹⁶ that relates the reaction rate of the electron probe reaction (v_e) to the concentration of photogenerated electrons at the SEI ($[e_{light}^-]$)

$$v_e = k_e [e_{light}^-] \quad \text{Eq. S18}$$

where k_e is the effective rate constant that reflects the surface electron activity, and has a unit of $s^{-1} m^{-2}$; note k_e depends on the electron-probe concentration in the solution, which is kept at 50 nM. The V dependence of $[e_{light}^-]$ is given by the Reichmann's expression²¹ for photogenerated majority carriers that diffuse in opposition to the electric field to the semiconductor/electrolyte interface rather than drift to the back contact:

$$[e_{light}^-] = \frac{P}{(v_c + \mu_n E_0) \left(1 + \frac{E_0}{\alpha V_{th}} \right)} \quad \text{Eq. S19}$$

where μ_n is the electron mobility, and v_c is the majority carrier collection velocity that reflects the effect of recombination in the space-charge region. E_0 is the absolute magnitude of the electric field at the SEI, which is given by

$$E_0 = \sqrt{\frac{2qN_D}{\epsilon_0 \epsilon_r} (V - V_{FB})} \quad \text{Eq. S20}$$

The kinetic model above (Eq. S18 - Eq. S20) contains two fitting parameters, k_e and V_{FB} . k_e reflects the intrinsic activity of photogenerated electrons in the semiconductor material that can diffuse to the surface, independent of light intensity and applied potential.

Since the derivation of Eq. S18 - Eq. S20 assumes that every absorbed photon produces an electron that can diffuse to the interface rather than drift to the back contact (i.e., the electron-hole separation efficiency is unity), k_e also contains contribution from the actual charge separation efficiency (i.e., η_{sep}). Because more efficient electron-hole separation would result in a larger quantity of electrons that drift to the back contact and thus a smaller quantity of electrons that can diffuse to the interface against the electric field, a material system with a higher η_{sep} value would be manifested by a smaller k_e value. Because ν_h and ν_e were measured on the same particle at the same subfacet location with identical intrinsic material properties (e.g., V_{FB}), $\nu_h - V$ and $\nu_e - V$ data were fitted globally with k_h , k_e , and shared V_{FB} as the fitting parameters (Fig. S13, e/h and f/i). The values of physical constants and material parameters of BiVO_4 used in fitting $\nu_h - V$ and $\nu_e - V$ relationships are listed in Table S1.

1.8 Light attenuation correction for subfacet-level photocurrents and carrier reaction rates on the {110} facet

In our subfacet-level photocurrent mapping and charge carrier reaction imaging experiments, the incident 405-nm laser travels in a direction that is passing the BiVO_4 particle first and then reaches the ITO electrode (Fig. S3, d and e). The light intensity at the top {010} facet and the top {110} facet is equal. However, the light intensity at the bottom {110} facet is different from that at the top facets due to the significant absorption of 405-nm light by the BiVO_4 particle (the value of absorption coefficient is shown in Table S1). Also, the light intensity at the bottom basal {010} facet is different from that at the top facets but it does not require correction since the bottom basal {010} facet, which is in direct contact with the ITO, is not accessible by the electrolyte or the reaction solution (Fig. S3, d and e), and therefore does not participate in producing photocurrents or catalyzing hole/electron probe reactions. In order to compare faithfully the photoelectrochemical properties between the {010} and {110} facets, we need to consider only the photocurrent and the reactions from the top {010} and {110} facets. In other words, the spatially resolved photocurrent (i_{ph}) and the specific hole/electron probe reaction rates (i.e., ν_h and ν_e) measured on the {110} facet needs to be corrected by light attenuation correction factors, in order to factor out the photocurrents and the reactions from the bottom {110} facet. We define $R(x)$ as the ratio of light intensity between the bottom and top {110} facets with the x -coordinate defined in Fig. S3 (also, see Main Text Fig. 1b). Note that we define $x > 0$ being on the {010} facet and $x < 0$ being on the {110} facet. Understandably this ratio is dependent on x since at different x values the vertical distance H (Fig. S3, e) for the light attenuation is different. Based on the Lambert-Beer law, $R(x)$ is given by

$$R(x) = \exp(-\alpha H) = \exp\left[-\sqrt{2}\alpha(L_{\{110\}} + x)\right] \quad \text{Eq. S21}$$

where α is given in Table S1, and $L_{\{110\}}$ is defined in Fig. S3 (also, see Main Text Fig. 1b) and is known for each particle. The light attenuation correction factor (f_{ph}) for a quantity measured at any subfacet location x (e.g., i_{ph} , ν_h , ν_e ; main text Fig. 1g-h) on the {110} facet is thus given by

$$f = \frac{1}{1 + R(x)} \quad \text{Eq. S22}$$

All the as-measured local quantities on the {110} facet of a particle (i.e., subfacet-level photocurrents discussed in Section 1.2, and specific hole/electron probe reaction rates on dissected segments discussed in Section 1.6) are corrected by multiplication by the light attenuation correction factor.

1.9 Calculation of experimentally measured single-whole-particle photocurrent density

The measured photocurrent by an iris-confined illumination (Fig. S6, mode III; see Methods in main text) for a single whole particle contains contributions from one top {010} facet, four top {110} facets and

four bottom {110} facets (Fig. S3 d and e). The top {010} and {110} facets have the same light intensity as measured experimentally, but the bottom {110} facets have significantly attenuated light intensities. To faithfully evaluate the photoelectrochemical performance of BiVO₄, the photocurrent density should only contain the contributions from the top {010} and {110} facets that experience the actual experimentally measured light intensity. For any particle with known $L_{\{010\}}$ and $L_{\{110\}}$, the ratio (r_1) of photocurrent contributions between the four bottom {110} facet and the four top {110} facet, and the ratio (r_2) of photocurrent contributions between the one top {010} facet and the four top {110} facets can be fully determined. Then, the true photoelectrochemical performance metrics for a whole particle (i.e., the photocurrent density for a whole particle, $j_{\text{ph}}^{\text{whole}}$) should be the contributions from only the top facets is

simply the directly measured photocurrents ($i_{\text{ph}}^{\text{measured}}$) multiplied by $\frac{1+r_2}{1+r_1+r_2}$ and divided by the total surface of the top facets (S_{top}):

$$j_{\text{ph}}^{\text{whole}} = i_{\text{ph}}^{\text{measured}} \times \frac{1+r_2}{1+r_1+r_2} \times \frac{1}{S_{\text{top}}} \quad \text{Eq. S23}$$

r_1 can be readily calculated by integrating the degree of light attenuation over the entire $L_{\{110\}}$ range (Section 1.8), and is given by

$$r_1 = \frac{L_{\{110\}}}{L_{\{110\}} + \int_0^{L_{\{110\}}} R(L_{\{110\}} + x) dx} \quad \text{Eq. S24}$$

where the functional form of $R(x)$ is given in Eq. S21. r_2 can be calculated by integrating the local photocurrent density ($j_{\text{ph}}^{\text{local}}(x)$), fully determined by the $L_{\{010\}}$ and $L_{\{110\}}$ values; Section 2.7 and Fig. S5 a-i) over the $L_{\{010\}}$ range and the $L_{\{110\}}$ range, respectively, and is given by

$$r_2 = \frac{\int_0^{L_{\{010\}}} j_{\text{ph}}^{\text{local}}(x) \text{Pr}(x) dx}{\int_{-L_{\{110\}}}^0 j_{\text{ph}}^{\text{local}}(x) \text{Pr}(x) dx} \quad \text{Eq. S25}$$

where the functional form of $\text{Pr}(x)$ is given in Eq. S29.

2 Control experiments and additional discussions/analyses

2.1 Energy-level analysis shows that the photogenerated holes and electrons in BiVO₄ can thermodynamically oxidize the hole-probe (amplex red) and reduce the electron-probe (resazurin), respectively

The theoretical positions of the conduction band edge (E_{CB}) and the valence band edge (E_{VB}) of BiVO₄ are ~ 0 V and 0.25 V versus the RHE electrode, respectively⁶. The peak oxidation potential of the hole-probe amplex red ($E_{\text{p, AR}}$) and the peak reduction potential of the electron-probe resazurin ($E_{\text{p, RZ}}$) are 1.01 V and 0.43 V versus RHE, respectively¹⁶. Therefore, E_{VB} of BiVO₄ is more positive than $E_{\text{p, AR}}$, and E_{CB} of BiVO₄ is more negative than $E_{\text{p, RZ}}$ (Fig. S10b), and therefore thermodynamically photogenerated holes and electrons in BiVO₄ can oxidize the hole-probe (amplex red) and reduce the electron-probe (resazurin), respectively. The red and blue arrows in Fig. S10b schematically illustrate the energetically possible pathways of photogenerated holes and electrons to amplex red and resazurin, respectively.

2.2 Ensemble results and ensemble-averaged single-particle results show that BiVO₄ can photoelectrocatalytically oxidize the hole-probe and reduce the electron-probe to generate the product molecule resorufin, and the rates of hole/electron probe reactions are negligible under the dark condition (i.e., without 405-nm illumination to generate charge carriers in BiVO₄)

We performed bulk-level photoelectrocatalytic kinetics of oxidative hole-probe reaction (i.e., amplex red oxidation) and reductive electron-probe reaction (i.e., resazurin reduction) (Fig. S10a) using a bulk BiVO₄ photoelectrode, in a three-electrode quartz cell with the initial concentration of amplex red or resazurin of 50 or 33 μM and a background electrolyte solution that consists of deaerated 0.1 M Na₂SO₄, 0.1 M pH 7.4 phosphate buffer. The bulk reaction kinetics was measured by tracking the fluorescence intensity at 585 nm in the emission spectra of the reaction solution, which scales with the concentration of the product molecule resorufin from either hole-probe or electron-probe reaction. We performed kinetic measurements by applying two different potentials of (0.43 and 0.93 V) under illumination with an expanded 405-nm laser beam with a power density of 16.6 mW cm⁻². For the hole-probe reaction, at a potential of 0.93 V, there is significant increase in the fluorescent intensity over time (Fig. S10c top curve), indicating that amplex red molecules are indeed oxidized, leading to effective generation of the fluorescent product molecule. At a less anodic potential of 0.43 V (Fig. S10c middle curve), the reaction also occurs but at a slower rate, which is expected for an oxidation reaction. Under the dark condition (Fig. S10c bottom curve), there is no significant amplex red oxidation. For the electron-probe reaction, it also occurs under photoelectrocatalytic conditions, but this potential-dependent trend is reversed. Note here the overall current is photoanodic but reductive reactions can still occur on the electrode surface because of a finite population of photogenerated electrons on the surface. At a less anodic potential of 0.43 V, there is also significant increase in the fluorescent intensity over time (Fig. S10d top curve), indicating that resazurin molecules are indeed reduced, leading to effective generation of the fluorescent product molecule. At a more anodic potential of 0.93 V (Fig. S10d middle curve), this reaction also occurs but at a slower rate, which is expected for a reduction reaction. Under the dark condition (Fig. S10d bottom curve), there is no significant resazurin reduction reaction.

Furthermore, we calculated the ensemble-averaged hole-probe reaction rates (Fig. S10e) and electron-probe reaction rates (Fig. S10f) at a series of applied potentials from 0.23 to 1.13 V. It is clear that the hole-probe reaction rate increases with increasing potential while the electron-probe reaction rate decreases with increasing potential. All these results confirm that BiVO₄ indeed can photoelectrocatalytically oxidize the hole-probe and reduce the electron-probe to generate the product molecule resorufin.

2.3 The hole and electron probe reactant molecules adsorb to all surface sites equivalently on the entire catalyst particle (i.e., no preferential adsorptions on certain facets, edges, corners or other subparticle regions)

To test whether the structurally similar hole and electron probe molecules, amplex red and resazurin (Fig. S10a), sample all surface sites in an unbiased way, we analyzed the residence time of the reaction product molecule resorufin (which is also structurally similar to the reactants amplex red and resazurin; Fig. S10a) at all the subparticle locations. For the hole-probe reaction, using the BiVO₄ particle in main text Fig. 1d as an example, we calculated the average residence time of the product molecule ($\langle t_{\text{res}} \rangle$) in each binned segment ($37 \times 37 \text{ nm}^2$) based on all the single product molecules detected at three anodic potentials combined (0.93 to 1.13 V). For the electron-probe reaction, we calculated the average residence time of the product molecule time based on all the single product molecules detected at five less anodic potentials combined (0.23 to 0.53 V). This average residence time is a good measure of how strongly resorufin, and presumably amplex red and resazurin, adsorb on surface sites. The mapping of $\langle t_{\text{res}} \rangle$ for the hole-probe reaction (Fig. S11a) shows a uniform spatial distribution, in contrast to the corresponding surface hole activity map (main text Fig. 1e). Additionally, the mapping of $\langle t_{\text{res}} \rangle$ for the electron-probe reaction (Fig. S11b) shows a uniform spatial distribution, in contrast to the corresponding surface electron activity map

(main text Fig. 1f). Furthermore, we calculated the averaged values of t_{res} from all the detected product molecules from single-molecule events in several representative subparticle regions (Fig. S11e), including the of the {010} facet (orange), the {110} facet (green), the edge region (red), and the four corner regions (I – IV, blue). The number of product molecules detected within each of these subparticle regions for the hole-probe and electron-probe reactions is shown in Fig. S11 f and i, respectively, and the corresponding averaged t_{res} values are shown in Fig. S11 g and j, respectively. Importantly, the averaged t_{res} values are very similar in all these regions. Overall, our residence time analysis results (Fig. S11 a, b, g and j) indicate that across different subparticle regions, the average residence time of resorufin is essentially the same, and is independent of the subparticle location, even though different subparticle regions differ markedly in terms of their reaction rates (main text Fig. 1 e and f). Such analyses here confirm that resorufin, and presumably amplex red and resazurin, do not preferentially adsorb onto certain facets, edges, corners, or other subparticle regions.

2.4 In our charge carrier reaction imaging, illumination is spatially uniform and reaction products have spatially uniform fluorescence intensities, and thus there is no spatially biased detection

The charge carrier reaction imaging experiments (for details, see Methods and 1.4) were performed with 405-nm/532-nm two-laser epifluorescence illumination and the two lasers were aligned and combined via a long-pass dichroic mirror to illuminate individual BiVO_4 particles dispersed on an ITO electrode in an epi-illumination geometry over an $70 \times 60 \mu\text{m}^2$ area. During the imaging experiments, typically only one or two BiVO_4 particles of interest were placed at the central region of the illuminated region. To determine whether the illumination is spatially uniform, we captured an image of the weak emission from the bare ITO electrode illuminated by 405-nm laser (Fig. S4 a), and the local emission intensity of this image reflects the magnitude of the local laser power density. The corresponding heat map of this emission image (Fig. S4 b) immediately shows that the illumination is highly uniform. We further analyzed the emission intensity distributions of a selected $40 \times 30 \mu\text{m}^2$ region at the center of the illuminated area (green box, Fig. S4 a) as well as of a dark region with no illumination (magenta box, Fig. S4 a). Both regions have similar degrees of uniformity in terms of their intensity spatial distributions (Fig. S4 c), which indicates that the illumination in our experiments is already as spatially uniform as is the dark condition. Notes that the BiVO_4 particles measured in our chemical imaging experiments have an overall particle size ranging from ~ 1 to $\sim 8 \mu\text{m}$, which is significantly smaller than the size of the region ($40 \times 30 \mu\text{m}^2$) with uniform illumination.

Furthermore, we analyzed the spatial distribution on a single particle of the average product molecule fluorescence intensity. For the hole-probe reaction, using the BiVO_4 particle in main text Fig. 1d as an example, we calculated the average product molecule fluorescence intensity ($\langle I_{\text{FL}} \rangle$) in each binned segment ($37 \times 37 \text{ nm}^2$) based on all the single product molecules detected at three anodic potentials combined (0.93 to 1.13 V). For the electron-probe reaction, we calculated the average product molecule fluorescence intensity based on all the single product molecules detected at five less anodic potentials combined (0.23 to 0.53 V). This average product molecule fluorescence intensity is a good measure of the actual local laser power density and a direct reflection of detection efficiency in single-molecule imaging. The mapping of $\langle I_{\text{FL}} \rangle$ for the hole-probe reaction (Fig. S11c) shows a uniform spatial distribution, in contrast to the corresponding surface hole activity map (main text Fig. 1e). Additionally, the mapping of $\langle I_{\text{FL}} \rangle$ for the electron-probe reaction (Fig. S11d) shows a uniform spatial distribution, in contrast to the corresponding surface electron activity map (main text Fig. 1f). Furthermore, we calculated the averaged values of I_{FL} from all the detected product molecules from single-molecule events within several representative subparticle regions (Fig. S11e), including the of the {010} facet (orange), the {110} facet (green), the edge region (red), and the four corner regions (I – IV, blue). The number of product molecules detected within each of these subparticle regions for the hole-probe and electron-probe reactions is shown in Fig. S11 f and

i, respectively, and the corresponding averaged I_{FL} values are shown in Fig. S11 h and k, respectively. We found that the averaged I_{FL} values are essentially the same across all these regions (Fig. S11 h and k).

Overall, our analysis of I_{FL} (Fig. S11 c, d, h and k), together with the results that show uniform laser illumination (Fig. S4 a-c), indicate that in our imaging measurements there is no spatially biased detection of the charge-carrier reactions on each particle.

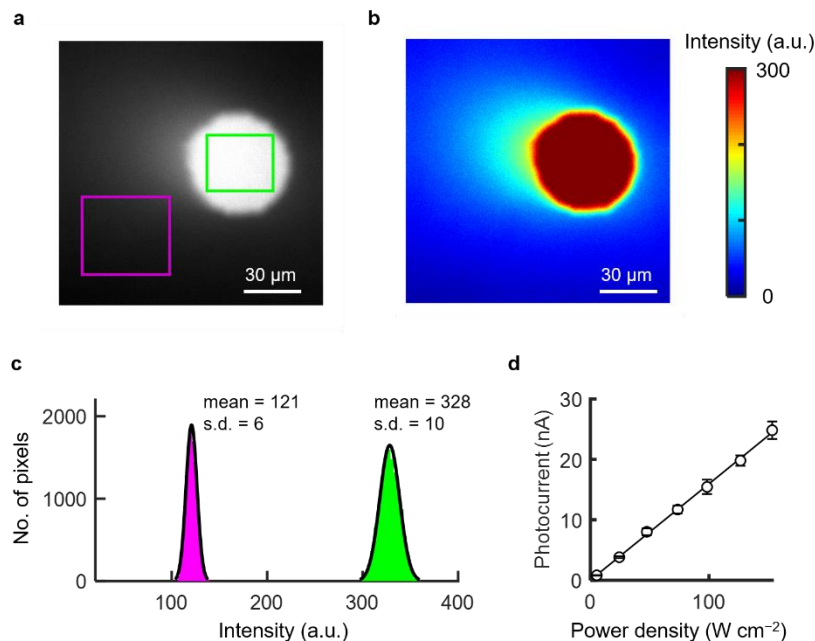


Fig. S4. Single-whole-particle photocurrent measurement with iris-confined epifluorescence illumination. (a) Representative image (512 by 512 pixels) of the weak emission from a bare ITO electrode with iris-confined 405-nm laser epifluorescence illumination (power density: 56 W cm^{-2}). The round periphery of the white region reflects the presence of an iris placed at the back port of the microscope to adjust the area of the illumination region (Fig. S6, mode III). (b) Heat map of the emission image in a. (c) Histograms of the emission intensities of the pixels in the dark area (left; magenta box in a) and in the bright area (right; green box in a). Black line: fit with a normal distribution. (d) Representative 405-nm laser power density dependences of single-whole-particle photocurrents measured at a potential of 1.13 V, showing a linear correlation between photocurrents and laser power densities. Solid line: fit with a linear function.

2.5 For inter-facet edges with no inter-facet junction effect (i.e., edge formed between two identical $\{110\}$ facets), there is no micrometer-sized spatial variation of hole/electron probe reaction rates

To test whether the observed micron-length-scale spatial variations of hole/electron probe reaction rates across the $\{010\}/\{110\}$ edge could potentially result from structural differences at these edges (e.g., low coordination surface sites) instead of the electronic effects of inter-facet junctions, we analyzed the spatial profile of reactions rates at the $\{110\}/\{110\}$ edges (Fig. S12a), which also have similar structural differences but do not have inter-facet junction effect because they are between identical facets. We calculate the spatial distribution of the number of detected product molecules (n_p) as a function of the distance away from the $\{110\}/\{110\}$ edge, for the eight regions (I – VIII) defined in Fig. S12a. We did not observe systematic micron-length-scale spatial variation of reaction rates at those $\{110\}/\{110\}$ edges in all the eight regions, for both the hole-probe reaction (Fig. S12b) and the electron-probe reaction (Fig. S12d). Averaging over all the eight regions (Fig. S12 c and e), it becomes even clearer that there is no monotonic decay/increase away from the $\{110\}/\{110\}$ edge to the facets. Please note that the hump at $\sim 500 \text{ nm}$ in Fig. S12b (region IV) or Fig. S12c is just for this particular particle as individual particles always show some spatial “hot spots”; the locations of such “hot spots” differ from one particle to another.

Altogether, these results demonstrate that for inter-facet edges with no inter-facet junction effect (i.e., edge formed with only $\{110\}$ facets with identical surface structure and energies), there is no micrometer-

sized spatial variation of hole/electron probe reaction rates. This confirms that the observed micron-length-scale spatial variations of hole/electron probe reaction rates at the {010}/{110} edge between two different types of facets are *not* due to structural defects at these edges (e.g., low coordination surface sites).

2.6 Modelling the facet size (i.e., $L_{\{010\}}$ and $L_{\{110\}}$) scaling laws of V_{FB} and η_{sep} at the {010}{110} inter-facet edge and intrinsic to the two facets

We modelled the two-dimensional facet size (i.e., $L_{\{010\}}$ and $L_{\{110\}}$) dependences of V_{FB} values (main text Fig. 2a) at the edge and intrinsic to the two facets (i.e., $V_{\text{FB,edge}}$, $V_{\text{FB},\{010\}}$ and $V_{\text{FB},\{110\}}$, which are defined in main text Fig. 1i) using the following equation:

$$y(L_{\{010\}}, L_{\{110\}}) = \beta_1 - \frac{\beta_2}{L_{\{010\}}} - \frac{\beta_3}{L_{\{110\}}} \quad \text{Eq. S26}$$

where y represents $V_{\text{FB,edge}}$, $V_{\text{FB},\{010\}}$ or $V_{\text{FB},\{110\}}$, and β_i ($i = 1, 2$ or 3) are positive scaling parameters (Table S2). The scaling relation of V_{FB} with the facet size $L_{\{010\}}$ or $L_{\{110\}}$ (i.e., $-\frac{\beta_2}{L_{\{010\}}}$ or $-\frac{\beta_3}{L_{\{110\}}}$) is based on the thermodynamic model that gives the size dependence of the particle surface energy^{22,23}. Such scaling behavior is applicable to particles containing more than 100 atoms (i.e., size is approximately larger than 10 nm), whose energy level splitting is much smaller than the thermal energy and the quantum size effects are negligible²²⁻²⁴. Hence, Eq. S26 is applicable to the BiVO_4 particles measured in our study (main text Fig. 2a), whose $L_{\{010\}}$ and $L_{\{110\}}$ ranges from ~ 400 to ~ 4000 nm.

We then modelled the two-dimensional facet size (i.e., $L_{\{010\}}$ and $L_{\{110\}}$) dependences of η_{sep} values (main text Fig. 2b) at the edge and intrinsic to the two facets (i.e., $\eta_{\text{sep,edge}}$, $\eta_{\text{sep},\{010\}}$ and $\eta_{\text{sep},\{110\}}$) using an empirical scaling relation based on the experimentally observed negative correlation between V_{FB} and η_{sep} (Fig. 1i; Fig. 2 a and b):

$$z(L_{\{010\}}, L_{\{110\}}) = \lambda_1 + \frac{\lambda_2}{L_{\{010\}}} + \frac{\lambda_3}{L_{\{110\}}} \quad \text{Eq. S27}$$

where z represents $\eta_{\text{sep,edge}}$, $\eta_{\text{sep},\{010\}}$ or $\eta_{\text{sep},\{110\}}$, and λ_i ($i = 1, 2$ or 3) are positive scaling parameters (Table S3).

Table S2. Values of the scaling parameters in the two-dimensional model that describes the $L_{\{010\}}$ and $L_{\{110\}}$ dependences of $V_{\text{FB,edge}}$, $V_{\text{FB},\{010\}}$, or $V_{\text{FB},\{110\}}$ (error bar: s.d.)

	β_1 (V)	β_2 (V nm)	β_3 (V nm)
$V_{\text{FB,edge}}$	0.47 ± 0.02	311 ± 22	67 ± 16
$V_{\text{FB},\{010\}}$	0.61 ± 0.02	311 ± 22	67 ± 17
$V_{\text{FB},\{110\}}$	0.36 ± 0.02	308 ± 21	71 ± 17

Table S3. Values of the scaling parameters in the two-dimensional model that describes the $L_{\{010\}}$ and $L_{\{110\}}$ dependences of $\eta_{\text{sep,edge}}$, $\eta_{\text{sep},\{010\}}$ or $\eta_{\text{sep},\{110\}}$ (error bar: s. d.)

	λ_1 (%)	λ_2 (% nm)	λ_3 (% nm)
$\eta_{\text{sep,edge}}$	2.2 ± 0.1	580 ± 78	116 ± 37

$\eta_{\text{sep},\{010\}}$	0.2 ± 0.0	587 ± 69	83 ± 32
$\eta_{\text{sep},\{110\}}$	14.7 ± 0.1	709 ± 118	215 ± 56

2.7 Quantitative prediction of decoupled, two-dimensional facet size (i.e., $L_{\{010\}}$ and $L_{\{110\}}$) dependences of single-whole-particle photocurrent densities

For any particle with specified $L_{\{010\}}$ and $L_{\{110\}}$, its V_{FB} and η_{sep} values (main text Fig. 2 a and b) at the edge and intrinsic to the two facets can be readily determined by the two-dimensional facet size scaling models (main text Fig. 2 a and b; for details, see Table S2, Table S3, Section 2.6), and $W_{\{010\}}$ and $W_{\{110\}}$ have known constant values independent of $L_{\{010\}}$ and $L_{\{110\}}$ (main text Fig. 2c). Therefore, using main text Eq. 1, for any particle with any combinations of $L_{\{010\}}$ and $L_{\{110\}}$, we can calculate the local values of V_{FB} and η_{sep} as a continuous function of the subfacet location x over the entire $L_{\{010\}}$ and $L_{\{110\}}$ ranges (Fig. S5 a-b, d-e, or g-h, for three differently shaped particles as examples). Next, using the modified Reichmann model for photocurrent predictions^{1,2} (Eq. S2 - Eq. S13; Section 1.3), we can determine the local photocurrent at any given potential as a continuous function of the subfacet location x , $i_{\text{ph}}^{\text{local}}(x)$ (Fig. S5 c, f, i), and immediately calculate the local photocurrent density ($j_{\text{ph}}^{\text{local}}(x)$) simply by division by the illumination area (i.e., $j_{\text{ph}}^{\text{local}}(x) = i_{\text{ph}}^{\text{local}}(x)/S_{\text{laser}}$, where S_{laser} is the area of the focused laser spot with a diameter of 380 nm, Section 1.1). Then, the whole-particle photocurrent density is the surface-area-weighted average of the local photocurrent density:

$$j_{\text{ph}}^{\text{whole}} = \frac{\int_{-L_{\{110\}}}^{L_{\{010\}}} j_{\text{ph}}^{\text{local}}(x) \text{Pr}(x) dx}{\int_{-L_{\{110\}}}^{L_{\{010\}}} \text{Pr}(x) dx} \quad \text{Eq. S28}$$

where $\text{Pr}(x)$ is the perimeter of the square that sits at the location of x (see particle dissection, Fig. S3a), and is given by

$$\text{Pr}(x) = \begin{cases} 8(L_{\{010\}} - x), & (x \geq 0) \\ 4\sqrt{2}(\sqrt{2}L_{\{010\}} - x), & (x < 0) \end{cases} \quad \text{Eq. S29}$$

Note that $\int_{-L_{\{110\}}}^{L_{\{010\}}} \text{Pr}(x) dx$ is simply the total surface area of the top facets (one top $\{010\}$ facet + four top $\{110\}$ facets (Fig. S3 d and e). Since the local photocurrents obtained here already contain corrections implicitly to only reflect the photocurrents from the top facets (Section 1.8) (because V_{FB} and η_{sep} values were obtained after light attenuation corrections), thus the area included in the calculations consistently only include the top $\{010\}$ and $\{110\}$ facets.

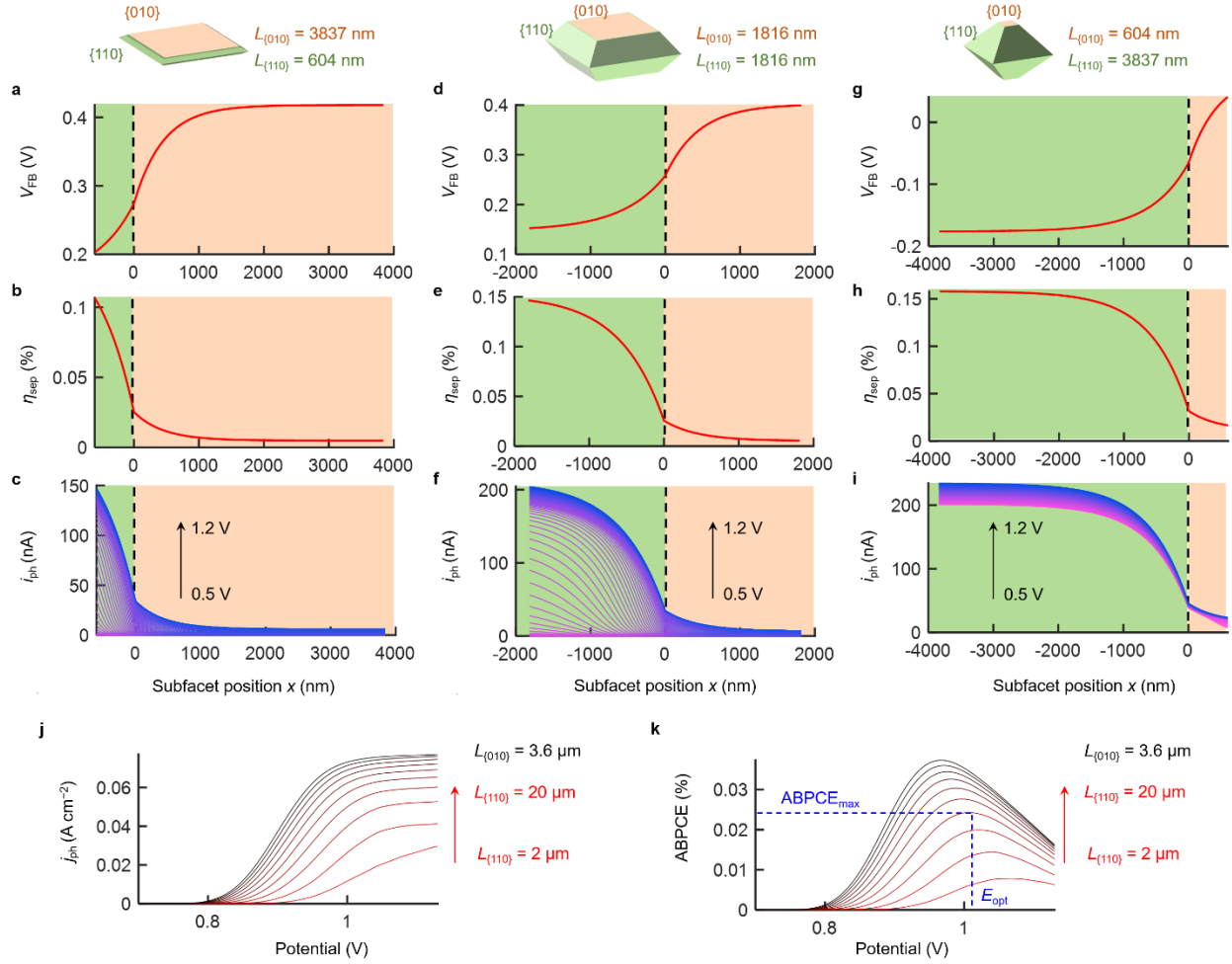


Fig. S5. Procedures for quantitative predictions of the $(L_{\{010\}}, L_{\{110\}})$ dependences of photoelectrode performance and operating conditions. (a – c) Calculated subfacet location dependences of flat-band potential (V_{FB}) (a), electron-hole separation efficiency in the SEI depletion zone (η_{sep}) (b), and the resulting subfacet-level photocurrents (i_{ph}) at many potentials (arrow indicates the potential varying from 0.5 to 1.2 V) (c), for a representative plate-like BiVO_4 particle with $L_{\{010\}} = 3837$ nm and $L_{\{110\}} = 604$ nm (for details on these quantitative predictions, see Section 2.7). (d – f) Same as a – c except for a truncated bipyramid-like BiVO_4 particle with $L_{\{010\}} = 1816$ nm and $L_{\{110\}} = 1816$ nm. (g – i) Same as a – c except for a bipyramid-like BiVO_4 particle with $L_{\{010\}} = 604$ nm and $L_{\{110\}} = 3837$ nm. (j, k) Predicated potential dependences of single-whole-particle photocurrent densities (j_{ph}) (j) for a series of particles with a fixed $L_{\{010\}} = 3.6$ μm and $L_{\{110\}}$ values varying from 2 to 20 μm , and the corresponding potential dependences of ABPCE (k) (the blue dashed lines indicate the definitions of maximally achievable ABPCE, $\text{ABPCE}_{\text{max}}$ and, the corresponding potential applied, E_{opt} , for $L_{\{110\}} = 8$ μm). For details, see Section 2.8.

2.8 Quantitative prediction of decoupled, two-dimensional facet size (i.e., $L_{\{010\}}$ and $L_{\{110\}}$) dependences of j_{ph} -vs.- V behavior and optimal operating condition of a whole particle

One of the most common performance metrics for photoelectrochemical water splitting devices is the applied-bias photon-to-current efficiency (ABPCE)^{6,25}, which is defined as

$$\text{ABPCE}(\%) = \frac{j_{\text{ph}} \times (V_{\text{H}_2\text{O}/\text{O}_2} - V)}{P} \times 100 \quad \text{Eq. S30}$$

where j_{ph} is the photocurrent density, $V_{\text{H}_2\text{O}/\text{O}_2}$ is the standard potential for water oxidation (1.23 V versus RHE), and P is the incident light power density. $j_{\text{ph}}^{\text{whole}}(L_{\{010\}}, L_{\{110\}})$ at any given potential can be obtained

from Eq. S28 (for details, see Section 2.7). So for any given combination of $L_{\{010\}}$ and $L_{\{110\}}$, we can determine the relationship between the photocurrent density j_{ph} and the applied potential V (Fig. S5 j), from which the ABPCE *versus* V relationship can be determined based on Eq. S30 (Fig. S5 k). Then, maximally achievable ABPCE, $\text{ABPCE}_{\text{max}}$, and, the corresponding potential applied, E_{opt} can be determined from the ABPCE - V curve (Fig. S5 k).

2.9 Determination of the surface dopant densities on the {010} and {110} facets based on experimentally measured V_{FB} spatial profiles across inter-facet junctions

Based on a theoretical model on electrostatics of lateral two-dimensional junctions²⁶, $W_{\{010\}}$ and $W_{\{110\}}$ of an inter-facet junction are related to the surface donor density on the {010} facet ($N_{\text{D},\{010\}}$) and the surface acceptor density on the {110} facet ($N_{\text{A},\{110\}}$) by the following equations:

$$W_{\{010\}} = \frac{N_{\text{A},\{110\}}}{N_{\text{A},\{110\}} + N_{\text{D},\{010\}}} \times \frac{\pi^2 \varepsilon_{\text{eff}} \Delta\varphi_{2\text{D}}}{qN_{\text{D},\{010\}} f\left(\frac{N_{\text{A},\{110\}}}{N_{\text{D},\{010\}}}\right)} \quad \text{Eq. S31}$$

$$W_{\{110\}} = \frac{N_{\text{D},\{010\}}}{N_{\text{A},\{110\}} + N_{\text{D},\{010\}}} \times \frac{\pi^2 \varepsilon_{\text{eff}} \Delta\varphi_{2\text{D}}}{qN_{\text{D},\{010\}} f\left(\frac{N_{\text{A},\{110\}}}{N_{\text{D},\{010\}}}\right)} \quad \text{Eq. S32}$$

where

$$f\left(\frac{N_{\text{A},\{110\}}}{N_{\text{D},\{010\}}}\right) = \sum_{k=1}^{\infty} \frac{\left[1 - (-1)^k\right] \left(1 + \frac{N_{\text{A},\{110\}}}{N_{\text{D},\{010\}}}\right) \sin\left(\frac{\pi k}{1 + \frac{N_{\text{A},\{110\}}}{N_{\text{D},\{010\}}}}\right)}{k^2} \quad \text{Eq. S33}$$

and ε_{eff} is the effective dielectric constant, and $\Delta\varphi_{2\text{D}}$ is defined in main text Fig. 1b. For each individual particle, with the multimodal imaging tools (Fig. S6; see Methods), we can experimentally determine $W_{\{010\}}$, $W_{\{110\}}$ and $\Delta\varphi_{2\text{D}}$ ($= q(V_{\text{FB}}^{\{010\}} - V_{\text{FB}}^{\{110\}})$) from the V_{FB} versus x spatial profile (Fig. 1i, red data). Then, by solving the set of coupled equations (Eq. S31, Eq. S32, Eq. S33), we can obtain the values of $N_{\text{D},\{010\}}$ and $N_{\text{A},\{110\}}$ for each individual particle. Notably, this is the first time that quantitative information of subparticle-level, facet-specific surface dopant density is obtained, due to our ability to visualize the spatial profile of V_{FB} across the {010}/{110} inter-facet edge on individual particles.

2.10 Calculation of the facet-specific near-edge surface transition zone width (i.e., $W_{\{010\}}$ and $W_{\{110\}}$) dependences of $L_{\{110\}}^{\text{level-off}}$

The $j_{\text{ph}}^{\text{whole}}$ *versus* ($L_{\{010\}}$, $L_{\{110\}}$) relationship (e.g., main text Fig. 2e) can be quantitatively predicted (for details, see Section 2.7), given: i) the values of $W_{\{010\}}$ and $W_{\{110\}}$ (both are independent of $L_{\{010\}}$ and $L_{\{110\}}$) (main text Fig. 2c), and ii) the two-dimensional ($L_{\{010\}}$, $L_{\{110\}}$) dependences of V_{FB} and η_{sep} at the inter-facet edge and intrinsic to the two facets (i.e., $V_{\text{FB}}^{\text{edge},\{010\}}$, $V_{\text{FB}}^{\{010\}}$, $V_{\text{FB}}^{\text{edge},\{110\}}$, $V_{\text{FB}}^{\{110\}}$, $\eta_{\text{sep}}^{\text{edge},\{010\}}$, $\eta_{\text{sep}}^{\{010\}}$, $\eta_{\text{sep}}^{\text{edge},\{110\}}$, $\eta_{\text{sep}}^{\{110\}}$; main text Fig. 2 a and b; Table S2, Table S3, Section 2.6). To systematically investigate how the combinations of $W_{\{010\}}$

and $W_{\{110\}}$ affect $L_{\{110\}}^{\text{level-off}}$ (its definition is shown in main text Fig. 3d), we vary the values of $L_{\{010\}}$ and $L_{\{110\}}$, while keeping the same values of other parameter as shown in Table S2, Table S3. Then we can generate $j_{\text{ph}}^{\text{whole}}$ versus ($L_{\{010\}}$, $L_{\{110\}}$) relationships (e.g., main text Fig. 2e) at any combination of $W_{\{010\}}$ and $W_{\{110\}}$. For each two-dimensional $j_{\text{ph}}^{\text{whole}}$ versus ($L_{\{010\}}$, $L_{\{110\}}$) relationship, we calculate one-dimensional $j_{\text{ph}}^{\text{whole}}$ - $L_{\{110\}}$ curve at any specified $L_{\{010\}}$, and thus determine the $L_{\{110\}}^{\text{level-off}}$ value at any specified $L_{\{010\}}$. In this way, we obtain the $L_{\{110\}}^{\text{level-off}}$ values at any given combination of $W_{\{010\}}$ and $W_{\{110\}}$ at any specified $L_{\{010\}}$ (e.g., main text Fig. 3e).

2.11 Analysis and discussion of the single molecule fluorescence imaging results on N₂-treated BiVO₄ particles

Super-resolution charge carrier reaction imaging of N₂-treated BiVO₄ (Supplementary Fig. 18 a-b) shows that hole- (electron-) induced reactions preferentially occur on the lateral {110} (basal {010}) facet, showing consistent facet dependence of anisotropic charge accumulation as observed in untreated BiVO₄ (Fig. 1e-f). More important, N₂-treated BiVO₄ also exhibits intra-facet spatial variations of hole/electron activities (Supplementary Fig. 18 a-b), indicative of the inter-facet junction effects. Moreover, such spatial patterns are not due to preferential adsorption of probe molecules at different subparticle regions. The average residence time of the product molecule ($\langle t_{\text{res}} \rangle$) shows a uniform spatial distribution for both hole-induced (Supplementary Fig. 18c) and electron-induced reactions (Supplementary Fig. 18d). While the number of product molecules detected differ across different subparticle regions (Supplementary Fig. 18 f and i), the corresponding averaged t_{res} values are very similar (Supplementary Fig. 18 g and j). These residence time analyses indicate that hole- and electron- probing reactant molecules, structurally similar to the produce molecule, adsorb to all surface sites equivalently on the entire N₂-treated BiVO₄ particle. Additionally, N₂-treated BiVO₄ does not exhibit spatial variations of hole and electron activities near the {110}/{110} edges where no inter-facet junction effects are present (Supplementary Fig. 18 h and k).

2.12 Stability of N₂-treated BiVO₄ particles under operating conditions

The work by Galli and Choi *et al.*²⁷ demonstrated that nitrogen-doped BiVO₄ exhibits a long-term stability of at least 50 h under operating conditions (i.e., during photoelectrochemical water oxidation). They showed that nitrogen-doped BiVO₄ exhibits highly stable anodic photocurrents for ~50 h with no sign of decay in a potassium phosphate buffer solution with a pH = 7.2, indicating that the N substitutions and oxygen vacancies in the oxide lattice are stable under illumination and electrochemical bias. They also demonstrated that nitrogen-doped BiVO₄ is compositionally stable after 30 h of photoelectrochemical water oxidation based on XPS measurements. Therefore, the N₂-treated BiVO₄ particles should be highly stable during the entire course of our multimodal functional imaging measurements, which lasts ~ 1 h for one region of interest (much shorter than 50 h). To further verify the stability of the nitrogen-doped BiVO₄ particles prepared here, we measured the photoelectrochemical currents associated with water oxidation using a nitrogen-doped BiVO₄ bulk photoelectrode film with an applied potential of 1.13 V (i.e., the most anodic, oxidative condition used in our study) in a phosphate buffer solution with a pH = 7.4 (i.e., the electrolyte solution we used for all our measurements), and observed that there is no decay at all of photocurrents for at least 2 h (Figure S19). This result supports that our nitrogen-doped BiVO₄ particles are highly stable over the period of our measurements and there is no particle stability issue that can affect any of our conclusions.

2.13 Effects of nitrogen doping on the electronic and photoelectrochemical properties of BiVO₄

Density functional theory (DFT) calculations to elucidate the effects of nitrogen doping on the photoelectrochemical properties of BiVO₄ have been performed in the previous work²⁷ by Giulia Galli (University of Chicago) and Kyoung-Shin Choi (University of Wisconsin-Madison) *et al.*, the procedure of which we followed in this work to prepare nitrogen-treated BiVO₄. Nitrogen doping in BiVO₄ directly results in N substitution and O vacancy generation. The DFT calculations by Galli and Choi *et al.*²⁷ systematically studied the effects of charge-balanced N incorporation (i.e., replacing three O²⁻ with two N³⁻) and O vacancies, separately and in combination, on the electronic band structure and charge transport properties of BiVO₄. To summarize, they performed a series of calculations corresponding to the following scenarios: BiVO₄ with 12.5% neutral O replaced with neutral N (1:1 substitution), BiVO₄ with 6% and 1.5% O vacancies by removing neutral O atoms, BiVO₄ with charge-balanced N substitution (9% O replaced with 6% N and 3% O vacancy), and BiVO₄ with N substitution and excess O vacancies (6% N and 6% O vacancy, where half of the O vacancies balance the charges of substitutional N atoms, and the other half offers additional electrons). The key findings based on their *ab initio* calculations are: i) the presence of O vacancies does not change the bandgap of BiVO₄, but causes local lattice distortions, and the formation of small polarons (calculated binding energy = ~0.5 eV), which is likely in oxides such as BiVO₄ that exhibit strong electron-phonon interaction^{28,29}; ii) N substitution moves upward the valence-band maximum (VBM) by ~0.2 eV, indicating a reduced bandgap and thus enhanced photon absorption; and iii) N substitution lowers the activation energy of small polarons by 1.1%, suggesting an increase in electron mobility by 25% based on the small polaron model^{29,30}. Overall, their computational results, also verified by their experimental measurements, show that the N₂ treatment enhances photon absorption, which should lead to higher photon-to-current conversion efficiencies, and increases majority carrier density and mobility in BiVO₄, which should shift downward flat-band potentials²⁷ and improve electron-hole separation efficiency. These findings are consistent with our results that N₂-treated BiVO₄ shows enhanced incident photon-to-current conversion efficiency (Fig. 3f, Fig. 4c), more negative flat-band potentials (Fig. 3a, top panels; Supplementary Fig. 7a), and higher SEI charge separation efficiency (Fig. 3a, bottom panels; Supplementary Fig. 7b).

Future directions for DFT calculations. Our key finding here is the inter-facet junction effect of faceted BiVO₄ particles. For N-doped BiVO₄ particles, our main conclusions are: (1) N-doping changes the widths ($W_{\{010\}}$, $W_{\{110\}}$) of near-edge surface transition zones on the constituent {010} and {110} facets (Fig. 3 a-b); (2) the changed transition zone widths lead to altered facet-size dependences of whole-particle photoelectrode performance (Fig. 3d-f); (3) on average, N-doped particles show enhanced photoelectrochemical performance. For conclusion 3, DFT calculations by Galli and Choi on bulk films with periodic boundary conditions provided insights into the underlying electronic mechanisms. For conclusions 1 and 2, the DFT calculations would have to calculate the entire single particle with different facets to probe the band bending along the particle surface across the inter-facet edge. As the surface transition zone widths are >2 microns, the size of the particle to be calculated would need to be at least in microns, comprising >10⁷ atoms. To our knowledge, this large size is beyond what DFT could handle (typically 10²-10³ atoms) even with super-computers. A minor conclusion derived from the altered $W_{\{010\}}$ and $W_{\{110\}}$ is that oxygen vacancies are more easily generated on {010} than on {110} facets. Here, DFT calculations could perhaps be performed on BiVO₄ slabs with {010} or {110} orientations using periodic boundary conditions, in which N-doping levels are systematically varied. Then at each doping level, one could calculate the cohesive energy of the oxygen atoms to determine if {010} and {110} facets would differ in energetics in losing oxygen (i.e., creating vacancies). On the other hand, previous DFT calculations on BiVO₄ slabs by Yang *et al.*³¹ already showed that the {010} facet is oxygen-terminated and its near-surface region has a higher oxygen density and longer Bi-O bonds than the {110} facet (Fig S9), which supports our conclusion of {010} facet being more prone to oxygen loss, as we discussed in the main text.

2.14 Discussion of the effects of cocatalysts and future research opportunities

To achieve highly efficient photoelectrochemical water splitting, the light-harvesting semiconductors usually need to be modified with cocatalysts for promoting the hydrogen evolution reaction (HER) and/or the oxygen evolution reaction (OER). While all our data here on BiVO₄ particles are without cocatalysts, it is of interest to discuss how the incorporation of cocatalysts affects the performance of faceted photocatalyst particles and their inter-facet junction effect, and how nanoscale operando (photo)electrochemical tools can help elucidate the role of catalysts at the semiconductor-cocatalyst interface.

To improve photoelectrochemical properties, BiVO₄ has been modified with various types of cocatalysts such as FeOOH, NiOOH, Co-Pi, RhO₂, Co₃O₄, Pt, MnO_x, PbO₂, and IrO₂³²⁻³⁴. While the physics of semiconductor-electrolyte interface is well developed, limited work has been performed to delineate the effects of cocatalysts on interface physics. The nature of many cocatalysts is often ill defined (e.g., many such cocatalysts are usually porous, heterogeneous hydrated and redox-active with mixed valences), and the physics of semiconductor-cocatalyst interface remains poorly understood. Our functional imaging techniques and the related analytic framework should help further the understanding of such technologically important but poorly characterized interfaces.

Our single-particle functional imaging tools may offer cleaner microscopic details of the semiconductor-cocatalyst interface than conventional bulk-level photoelectrochemical measurements, because we can investigate the local photoelectrochemistry and semiconductor-cocatalyst junction properties at the single-particle/single-facet level with well-defined structure, while in conventional experiments semiconductors are often polycrystalline, porous and/or nanostructured, exhibiting large structural heterogeneities and complicating the interpretation of experimental results. Moreover, the cocatalyst layer itself is often spatially non-uniform and consists of dispersed cocatalyst nanoparticles with different sizes, connectivities and even properties (e.g., forming either buried or adaptive junctions³⁵), resulting in large spatial variations in the behavior of the semiconductor-cocatalyst-electrolyte junction³⁶. Building on our previous work on depositing cocatalysts on single TiO₂ nanorods¹⁶, we should be able to selectively deposit OER and HER catalyst nanoparticles on either hole-accumulating {110} or electron-accumulating {010} facets with the multimodal functional imaging tools at our disposal, and we can also quantify the size and amount of cocatalysts by correlative optical microscopy-scanning electron microscopy measurements. This would allow us to study a single local semiconductor-cocatalyst junction with known quantitative structural information for both the semiconductor facet and the cocatalyst nanoparticle attached, and examine how the overall photoelectrochemistry of the whole-construct (i.e., a semiconductor microcrystal with cocatalysts deposited on selected facets) is related to the nature and spatial distribution of semiconductor-cocatalyst junctions.

Furthermore, our operando imaging tools may help provide a clearer answer to the exact functional role of cocatalysts in water-oxidizing photoanodes such as BiVO₄. Elucidating this role is a challenging task, and has remained an active area of debate. Several possible mechanisms³⁷⁻⁴³ of how cocatalysts improve overall photoanode performance have been proposed, such as i) favorably modulating band bending in the semiconductor but does not drive the OER directly, ii) improving charge separation in the semiconductor by collecting and storing photogenerated holes in the cocatalyst layer, and iii) simply enabling more facile OER kinetics without affecting any interface energetics. In general, conventional bulk-level measurements have fundamental limitations in dealing with heterogeneities and cannot easily decouple highly convoluted contributing factors. In contrast, with multimodal photoelectrochemical imaging tools, we could probe local photoelectrochemistry and clarify certain aspects of the cocatalyst functions. For example, in principle we potentially can i) directly measure if the local water oxidation current is either enhanced, suppressed, or not affected at all by the cocatalyst nanoparticle, ii) determine how cocatalysts change the local flat-band potential and modulate the interface energetics, and iii) examine how the spatial distributions of surface electron and hole activities and the inter-facet junction effects depend on the cocatalyst properties. These types of measurements may help clarify the role of cocatalysts to some extent and help reconcile some contradictory conclusions from literature. Ultimately, a holistic picture

Section 1.1), and the resulting local photocurrent associated with a specific subfacet location was recorded by the potentiostat (Fig. S1 e-h). In **mode II**, several dispersed BiVO₄ particles were subject to simultaneous 405-nm/532-nm two-laser wide-field epi-illumination, with the product molecules of hole- or electron-induced fluorogenic reactions (Fig. S10a) being localized individually at a super-resolution of ~40 nm (Fig. S2 d and e). In **mode III**, the entire surface of a single BiVO₄ particle was subject to an iris-confined 405-nm laser illumination (Fig. S4), allowing for detection of whole-particle photocurrent associated with a specific particle with known {010} and {110} facet sizes. Note the schematic is drawn upside down.

The reasons we employed a photoelectrochemical flow cell configuration in our multimodal functional imaging measurements are the following. First, using a flow cell allows us to easily switch solutions for multiple measurements performed on the same set of particles, as well as conveniently maintain a N₂ purged environment. The photocurrent mapping, hole reaction imaging and electron reaction imaging require the use of three different solutions (i.e., blank electrolyte, electrolyte with hole-probe amplex red, electrolyte with electron-probe resazurin) for the same batch of particles. N₂ purging is needed to remove O₂ from the flow cell, preventing the reaction of photogenerated electrons with O₂ and the subsequent formation of superoxide radicals, which could oxidize amplex red¹⁸, which is intended to be a hole-probe instead of an electron-probe. Second, the use of flow cells with a tunable flow rate ensures that the supply rates of reactants are significantly larger than their consumption rates, and therefore the reaction rate is determined by the surface activities instead of limited by reactant mass transport. Based on the optimized condition from our previous work¹⁶, we used a volumetric flow rate of 25 $\mu\text{L min}^{-1}$, which provide probe molecules at a supply rate of $\sim 1 \times 10^{10}$ molecules per second, much larger than the maximum product formation rate of $\sim 1 \times 10^7$ molecules per second, estimated based on the hole-probe oxidation reaction rate at the most positive potential of 1.13 V (Fig. 1h) and the fact that ~1% of the 0.5 cm² exposed surface area of ITO was covered by BiVO₄ particles. The photoelectrocatalytic reaction rates do not depend on the flow rate because the rates are not limited by mass transfer as discussed earlier. The photocurrents are also not affected by the flow rate because the photocurrents are dominated by water oxidation and the water content is independent of the flow rate.

The ITO electrodes we used in this study were purchased from Delta Technologies (Part Number: CB-50IN-0111), and have a sheet resistance of 5-15 Ω/sq , a nominal transmittance of > 85%, a nominal coating thickness of 120 – 160 nm, a surface roughness of <0.02 $\mu\text{m}/5 \text{ mm}$ (peak-to-peak), and an overall size of 25 \times 25 \times 1.1 mm. We cannot quantify the degree of heterogeneity in terms of the local electrical conductivity on the ITO electrode. However, the sub-particle location dependences of photoelectrochemical properties (Figure 1 g-j) should not be affected by such heterogeneity, if any, because the measured quantities at different sub-particle locations share the same particle-ITO contact. Such heterogeneity, if any, may contribute to the particle-to-particle variations in photoelectrochemical properties though. Therefore, when drawing conclusions about particle size effects (i.e., facet size effects), we pool results from many particles to average out the possible heterogeneities. In our experiments, we saw a few particles with very low photoelectrochemical activities during initial tests but most of these particles typically either detached from the ITO surface during measurements probably due to poor surface contacts, and they are amorphous particles, irregularly-shaped particles, or aggregates of very small particles. To remove such particles as much as possible, we optimized spin-coating conditions to disperse mostly well-shaped particles on the ITO surface and spin away amorphous/irregularly shaped particles that do not tend to sit firmly on ITO surface, used annealing to improve the contacts between the coated particles and the ITO electrode, and after assembling the flow cell, we use a very high volumetric flow rate (> of 500 $\mu\text{L min}^{-1}$) for a couple hours to wash away loosely bound particles.

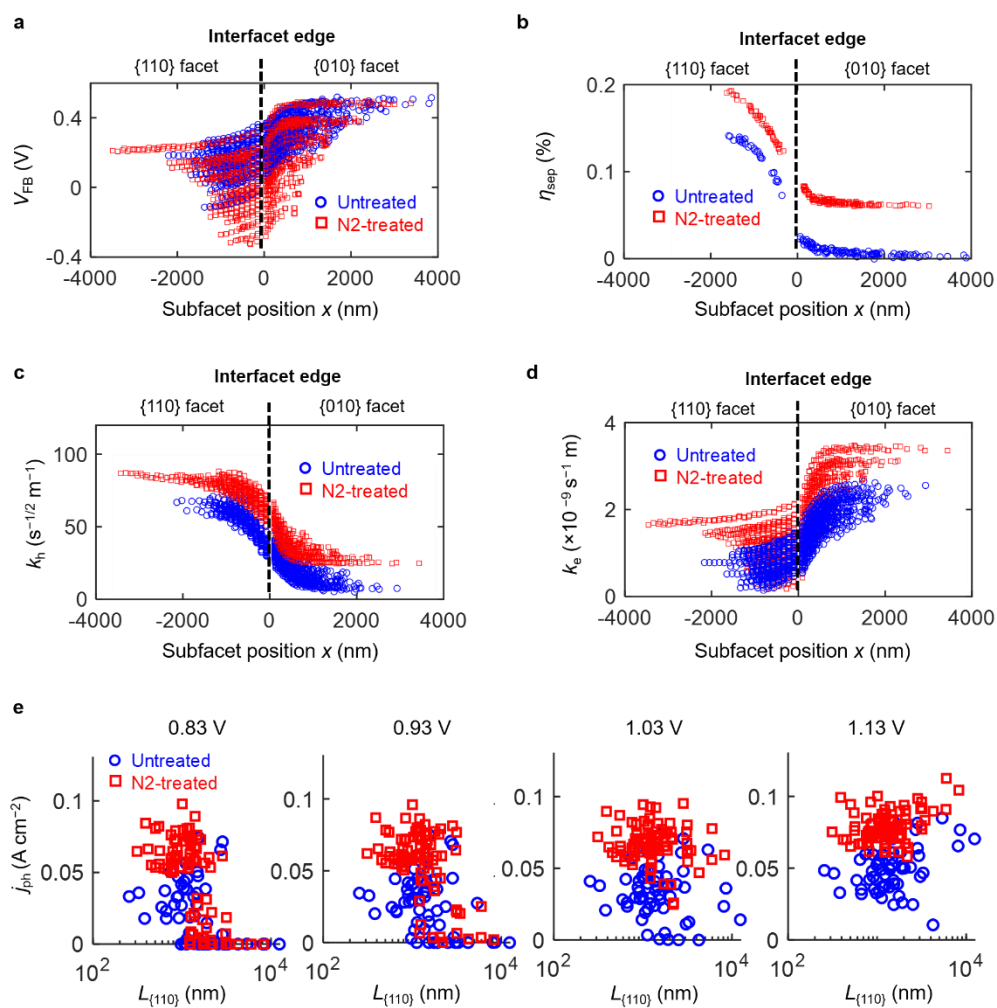


Fig. S7. Comparison of photoelectrochemical properties between untreated and N₂-treated BiVO₄. (a – d) Comparing intrinsic materials property parameters at all subfacet positions of all particles measured in this study (blue: untreated BiVO₄; red: N₂-treated BiVO₄): flat-band potential (V_{FB}) (a) (for details, see Sections 1.3 and 1.7), electron-hole separation efficiency in the SEI depletion zone (η_{sep}) (b) (for details, see Section 1.3), effective rate constants k_h (c) that reflects surface hole activities (for details, see Section 1.7), and effective rate constants k_e (d) that reflects surface electron activities (for details, see Section 1.7). (e) Comparing single-whole-particle photocurrent densities (j_{ph}) for all particles measured in this study (blue: untreated BiVO₄; red: N₂-treated BiVO₄) versus their $L_{\{110\}}$ values. Each point in e represents one particle.

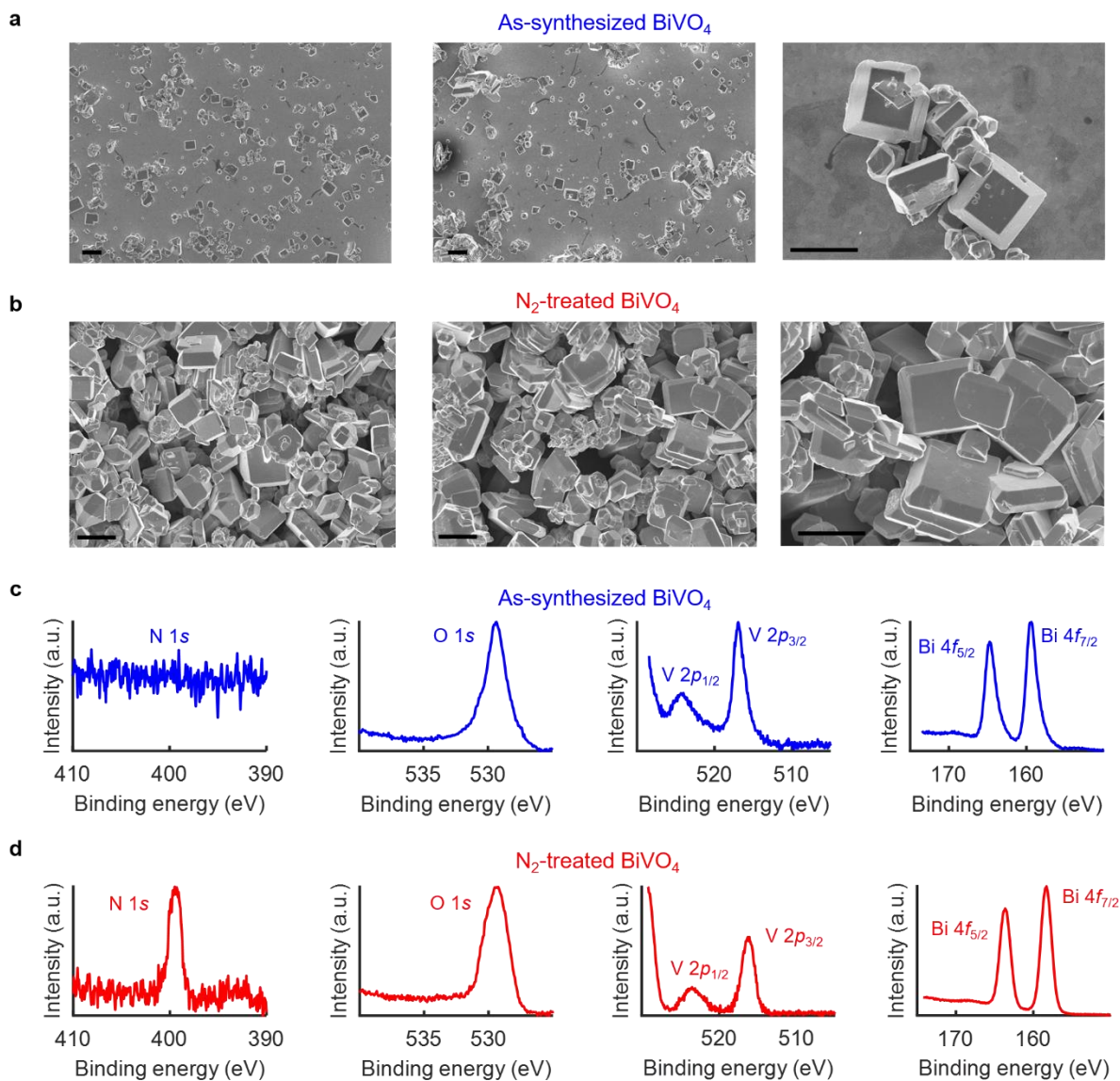


Fig. S8 Structural and compositional characterization of BiVO_4 and nitrogen-treated BiVO_4 . (a, b) Representative scanning electron microscopy images of as-synthesized BiVO_4 particles (a) and nitrogen-treated BiVO_4 particles (b). Scale bar: 10 μm in A; 5 μm in B. (c, d) High-resolution X-ray photoelectron spectra of N 1s, O 1s, V 2p, and Bi 4f for as-synthesized BiVO_4 particles (c) and nitrogen-treated BiVO_4 particles (d).

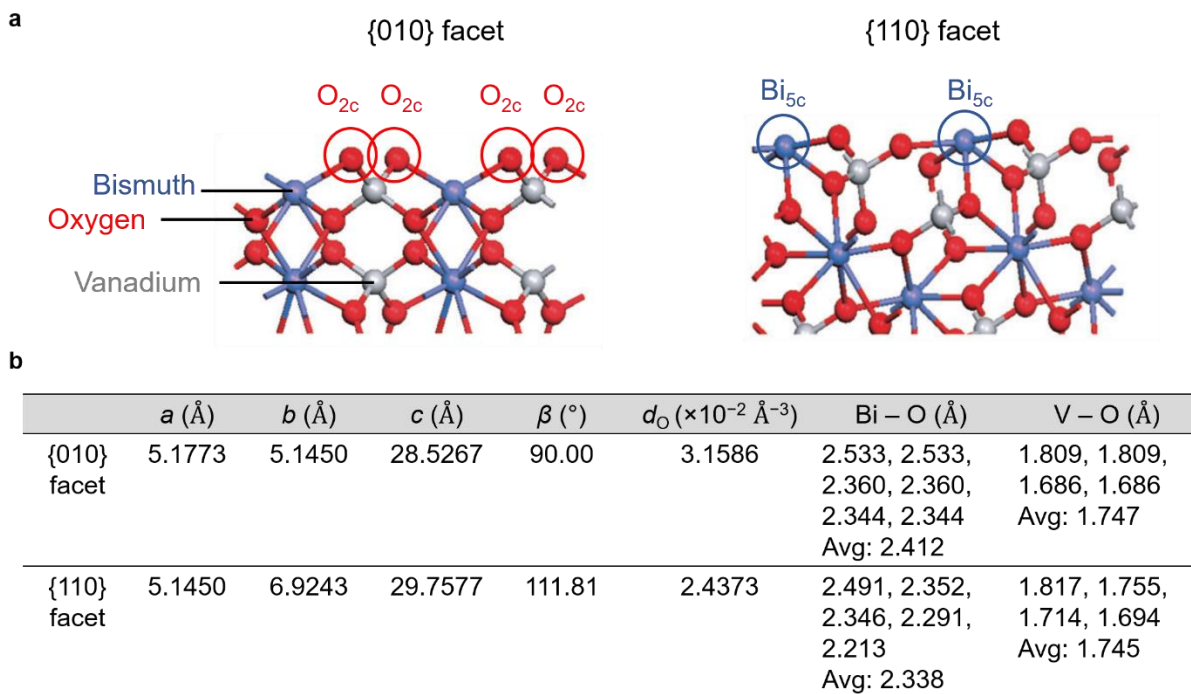


Fig. S9 Surface structures of monoclinic BiVO₄ {010} and {110} facets. (a) Calculated stable surface terminations of the {010} (left) and {110} facets (right)^{31,59,60}, reproduced from reference³¹ with permission from WILEY-VCH Verlag GmbH & Co. KGaA 2013. Bismuth: blue. Vanadium: gray. Oxygen: red. O_{2c}: 2-coordinated oxygen atom. Bi_{5c}: 5-coordinated bismuth atom. The {010} facet has stable surface terminations that are richer in 2-coordinated O²⁻ (electron donors) and has a lower energy level, while the {110} facet has stable surface terminations that are richer in 5-coordinated Bi⁵⁺ (electron acceptors) and has a higher energy level^{31,33}. (b) Calculated parameters of optimized {010} and {110} surface structures³¹, represented by slab models that contain six bismuth atom, six vanadium atoms, and 24 oxygen atoms. a , b , c and β : monoclinic crystal lattice parameters. d_o : oxygen atom volumetric density. Bi – O and V – O indicate the bond lengths between bismuth and oxygen, and between vanadium and oxygen, respectively. The average values (Avg) are also denoted.

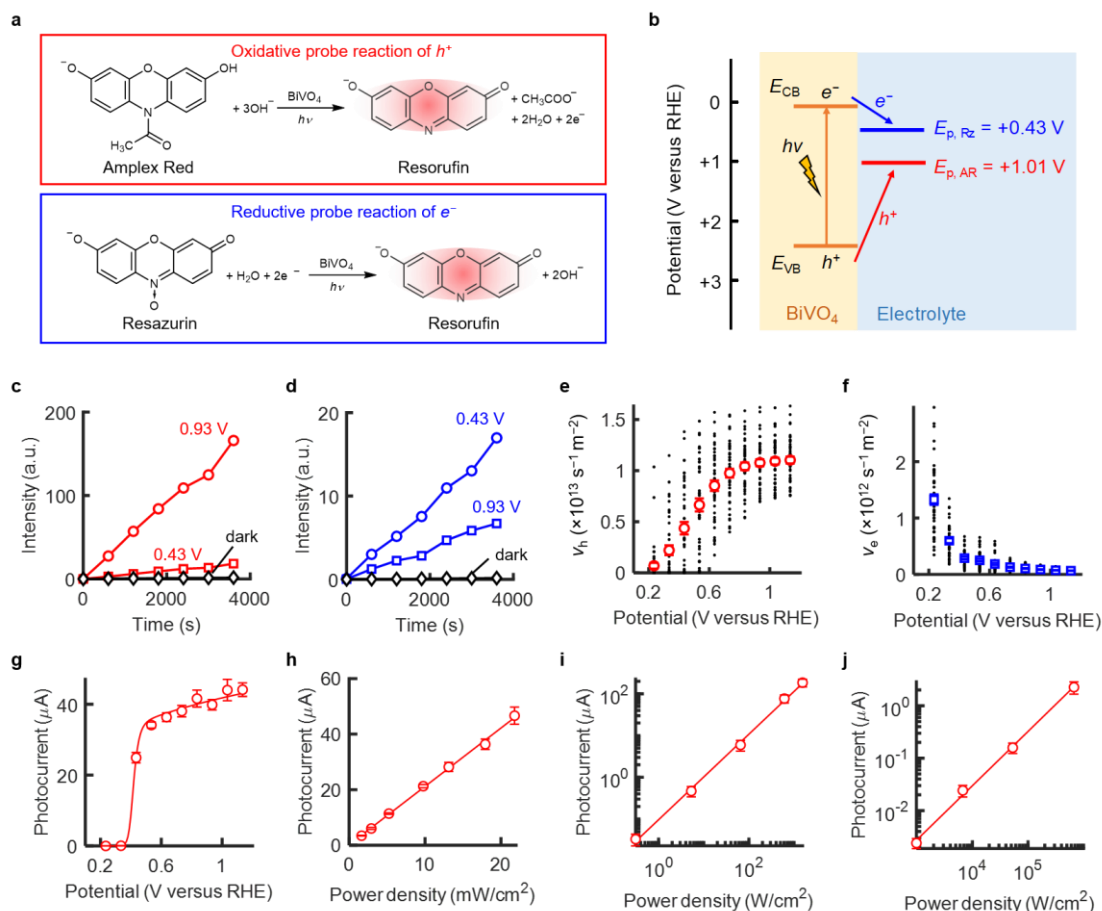


Fig. S10 Bulk and ensemble-averaged photoelectrochemical properties of BiVO_4 . (a) Oxidative N-deacetylation of nonfluorescent amplex red to highly fluorescent resorufin probes photogenerated holes while reductive N-deoxygenation of weakly fluorescent resazurin to highly fluorescent resorufin probes photogenerated electrons¹⁶. (b) Energy-level diagram (referenced to RHE) of the conduction band edge (E_{CB}) and the valence band edge (E_{VB}) of BiVO_4 ⁶, as well as the peak oxidation potential of amplex red ($E_{\text{p, AR}}$) and the peak reduction potential of resazurin ($E_{\text{p, RZ}}$)¹⁶. $h\nu$ indicates the incident light. The red and blue arrows schematically illustrate the energetically possible pathways of photogenerated holes and electrons to amplex red and resazurin, respectively. (c, d) Photoelectrocatalytic kinetics of oxidative hole-probe reaction (i.e., amplex red oxidation) (c) and reductive electron-probe reaction (i.e., resazurin reduction) (d) using a bulk BiVO_4 photoelectrode. The y-axis fluorescence intensity is the intensity measured at a given time minus that measured at time zero, and it scales with the concentration of the product molecule resorufin from either reaction generated from time zero. Initial concentrations of amplex red and resazurin are 50 and 33 μM , respectively, and the background electrolyte solution is deaerated 0.1 M Na_2SO_4 , 0.1 M pH 7.4 phosphate buffer. Illumination is done by an expanded 405-nm laser beam with a power density of 16.6 mW cm^{-2} . For hole-probe kinetic data in C, from top to bottom, the experimental condition is: applying a potential of 0.93 V with 405-nm illumination, 0.43 V with 405-nm illumination, and 0.93 V in the dark. For electron-probe kinetic data in D, from top to bottom, the experimental condition is: applying a potential of 0.43 V with 405-nm illumination, 0.93 V with 405-nm illumination, and 0.43 V in the dark. (e, f) Specific rates of hole-probe (e) and electron-probe (f) reactions as a function of the applied potential, measured in the photoelectrochemical microfluidic cell under our single-particle single-molecule imaging condition with wide-field two-laser illumination (405-nm laser power density: 12 W cm^{-2} ; 532-nm laser power density: 60 W cm^{-2}). Black dot: whole-particle specific reaction rate for one particle (total 45 particles). Squares: data averaged over the 45 particles. Error bar: s.e.m. (g) Representative potential dependence of photocurrents associated with water oxidation measured in a three-electrode configuration on a bulk BiVO_4 film in a front illumination configuration by an expanded 405-nm laser beam with a diameter of 2.4 cm and a power density of 21.2 mW cm^{-2} . The electrolyte is 0.1 M Na_2SO_4 , 0.1 M pH 7.4 phosphate buffer. Solid line is a fit with Eq. S2 (Supplementary Note 1.3) using k_{tr} and η_{sep} as floating parameters and a fixed theoretical value of V_{FB} (0.1 V versus RHE)⁴ for bulk BiVO_4 . This fitting yields a k_{tr} value of $1.4 \times 10^{-6} \text{ cm s}^{-1}$, in good agreement with the value ($2 \times 10^{-6} \text{ cm s}^{-1}$) previously obtained by scanning photoelectrochemical microscopy⁸. (h - j) Photocurrents versus 405-nm laser power densities measured in three illumination configurations using bulk BiVO_4 films deposited on ITO electrodes: with an expanded laser beam of a diameter of 2.4 cm in a quartz liquid cell (h), with wide-field (70 \times 60 μm^2) epifluorescence illumination in a microfluidic cell (i), and with a focused laser beam of a diameter of $\sim 380 \text{ nm}$ (Supplementary Note 1.1) in a microfluidic cell (j). Solid lines: linear fits. All error bars: s.d.

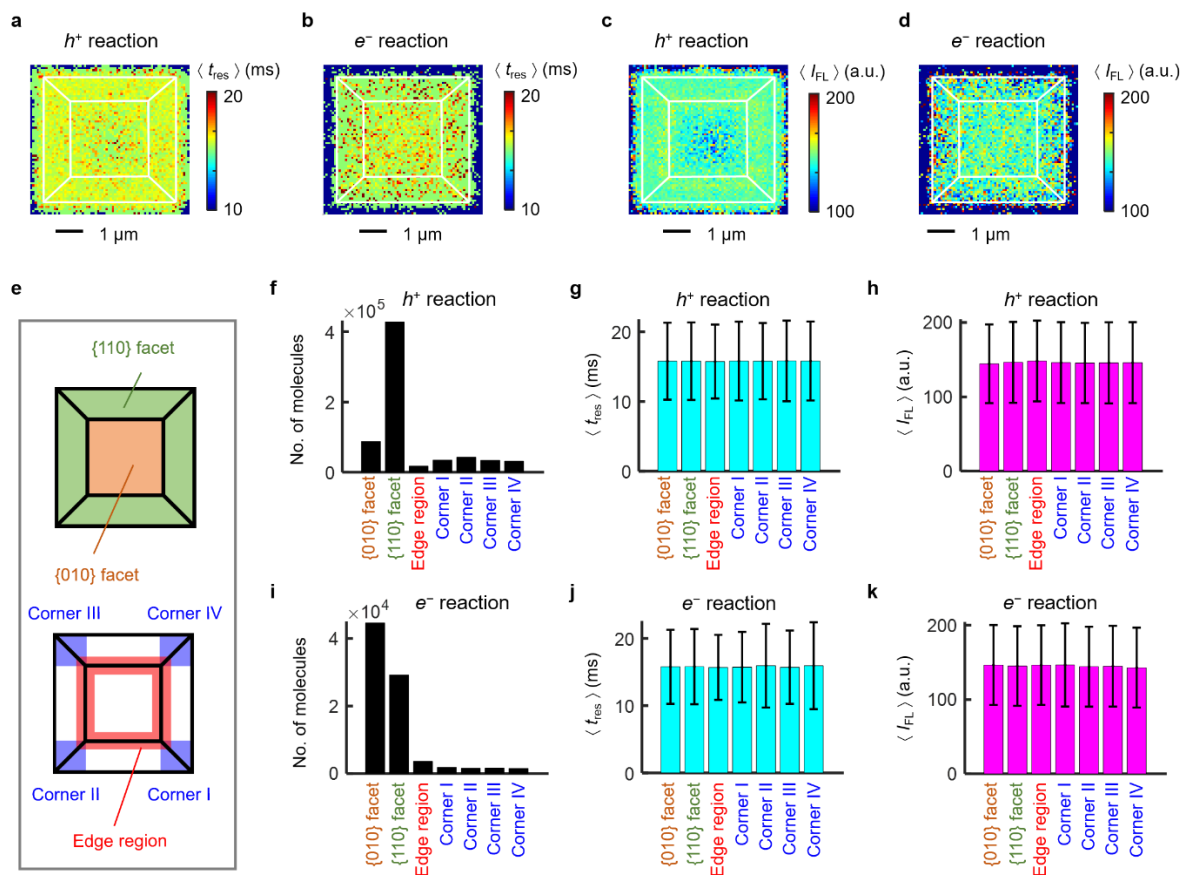


Fig. S11 Analyses of spatial distributions of residence time and single-molecule fluorescence intensity on single particles. (a) The spatial distribution of the average product molecule residence time ($\langle t_{\text{res}} \rangle$) on the BiVO_4 particle in main text Fig. 1d for the hole-probe reaction. Bin size: $74 \times 74 \text{ nm}^2$. Data here include single-molecule events detected at 0.93 to 1.13 V combined. (b) The spatial distribution of $\langle t_{\text{res}} \rangle$ of the same particle as in a for the electron-probe reaction. Bin size: $74 \times 74 \text{ nm}^2$. Data here include single-molecule events detected at 0.23 to 0.53 V combined. (c) The spatial distribution of the average product molecule fluorescence intensity ($\langle I_{\text{FL}} \rangle$) of the same particle as in a for the hole-probe reaction. Bin size: $74 \times 74 \text{ nm}^2$. Data here include single-molecule events detected at 0.93 to 1.13 V combined. (d) The spatial distribution of $\langle I_{\text{FL}} \rangle$ of the same particle as in a for the electron-probe reaction. Bin size: $74 \times 74 \text{ nm}^2$. Data here include single-molecule events detected at 0.23 to 0.53 V combined. (e) Illustrations of the {010} facet (orange), the {110} facet (green), the edge region (red), and the four corner regions (blue) for analyzing the t_{res} and I_{FL} values (f - k). For the edge region, the width on either side of the black ledge is chosen to be 40 nm, similar to our reaction imaging localization error ($\sim 40 \text{ nm}$) (Supplementary Fig. 2 d and e). (f - h) Number of detected product molecules (f), the averaged value of t_{res} (g), and the averaged value of I_{FL} (h) within each subparticle regions defined in e for the hole-probe reaction. Error bars in f and g: s.d. (i - k) Same as f-h, except for the electron-probe reaction.

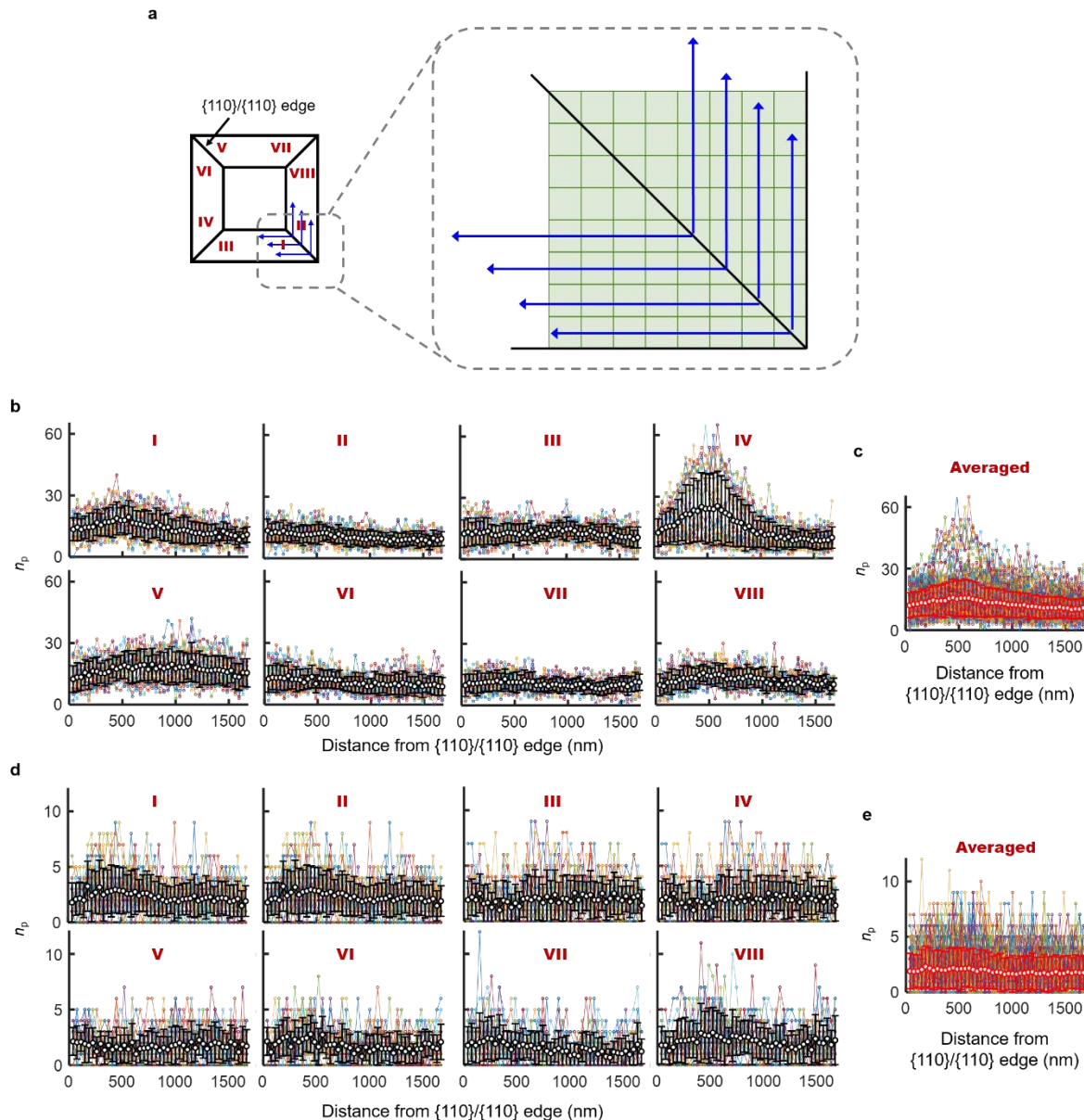


Fig. S12 Reactivity spatial distributions at the $\{110\}/\{110\}$ edge. (a) Schematic illustration of how to calculate the n_p (the number of product molecules generated in each bin in super-resolution h^+ or e^- reaction images, main text Fig. 1 e and f) distribution as a function of the distance away from the $\{110\}/\{110\}$ edge. One particle has eight subparticle regions (defined as I – VIII) near a $\{110\}/\{110\}$ edge. In the inset, each green box represents one $37 \times 37 \text{ nm}^2$ bin, which has a n_p value reflecting the h^+ or e^- activity. We plot the n_p value along each blue arrow as a function of the distance away from the $\{110\}/\{110\}$ edge (i.e., number of bins multiplied by the bin size, 37 nm), and the connected dots in different colors in b-e represent different line profiles along different blue arrows. (b) Hole-probe reaction n_p distribution as a function of the distance away from the $\{110\}/\{110\}$ edge for the eight regions (I – VIII) indicated in A calculated from the corresponding super-resolution h^+ reaction image (main text Fig. 1e). Data here include single-molecule events detected at 1.13 V. Each colored dot represents one $37 \times 37 \text{ nm}^2$ pixel in the super-resolution reaction image (i.e., a green box in a). Different colors indicate different horizontal or vertical line profiles along the blue arrows in a. Black circles are averaged over different line profiles. Error bar: s.d. (c) Data averaged over all the colored line profiles in all the eight regions in b. Colored dots here are compilation of all those from the eight subparticle regions (I – VIII) shown in b. Error bar: s.d. (d) Same as b, except for the electron-probe reaction data collected at 0.23 V (main text Fig. 1f). (e) Data averaged over all the colored line profiles in all the eight regions in d. Error bar: s.d. Colored dots here are compilation all those from the eight subparticle regions (I – VIII) shown in d.

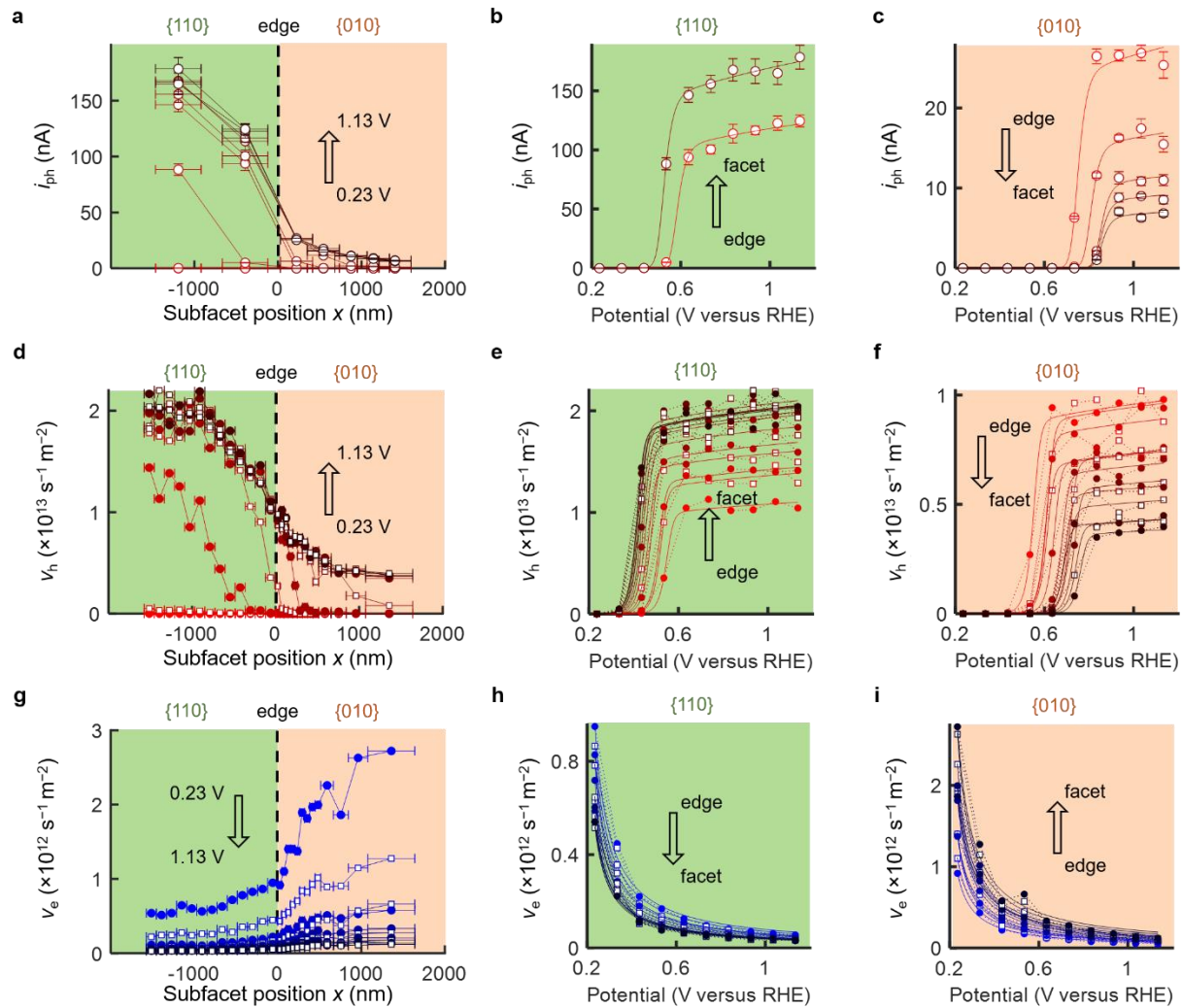


Fig. S13 Subfacet position- and potential-dependences of photocurrents (i_{ph}) (a - c) and hole or electron-induced reaction rates (v_h , v_e) (d - i). (a, d, g) Subfacet position dependence of i_{ph} (a), v_h (d) and v_e (g) at various applied potentials. The arrow indicates the applied potential varying from 0.23 to 1.13 V. (b, e, h) Potential dependence of i_{ph} (b), v_h (e) and v_e (h) at various subfacet locations (for b) or various dissected segments on the {110} facet (for e, h). The arrow indicates data near the inter-facet edge toward the bulk facet (i.e., away from the edge). (c, f, i) Same as b, e, h, except for the {010} facet. Solid lines in b and c: fits with Eq. S2 (Supplementary Note 1.3). Solid lines in e, f, h and i: fits with Eq. S16 and Eq. S18 (Supplementary Note 1.7). Dashed lines in e, f, h and i simply connect data obtained from the same dissected segment. All vertical error bar: s.d. (Supplementary Note 1.2). All horizontal error bar: resolution of measurement (Supplementary Note 1.1) or area dissection (Supplementary Note 1.6). All data in this figure were obtained on the particle discussed in main text Fig. 1d. Data presented in Fig. 1 g and h are part of the data shown here.

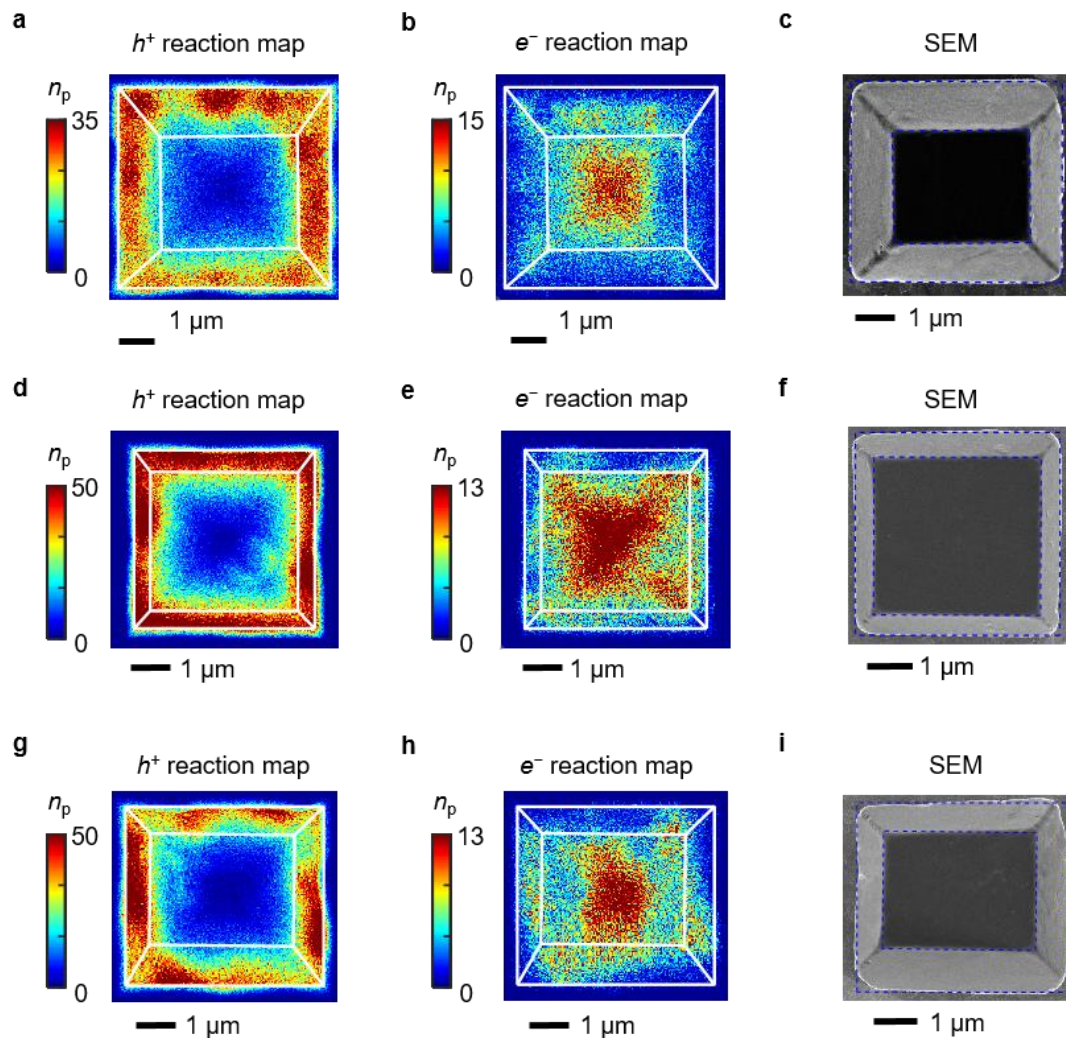


Fig. S14 Additional examples of charge carrier reaction imaging results on single BiVO_4 particles. (a, b) Super-resolution images of h^+ (potential ≥ 0.93 V) (a) and e^- (potential ≤ 0.63 V) (b) induced reactions (for details, see Methods and Supplementary Note 1.4) on the particle in c. n_p : number of detected reaction product molecules. Bin size: 36.3×36.3 nm². White lines: structural contours determined from the SEM image in c. Imaging duration at each potential: 22.5 min. (c) SEM of the particle in a and b in the same orientation. (d – f) Same as a – c except that bin size = 37.0×37.0 nm² for a different particle shown in f. (g – i) Same as a – c except that bin size = 35.8×35.8 nm² for another particle shown in i.

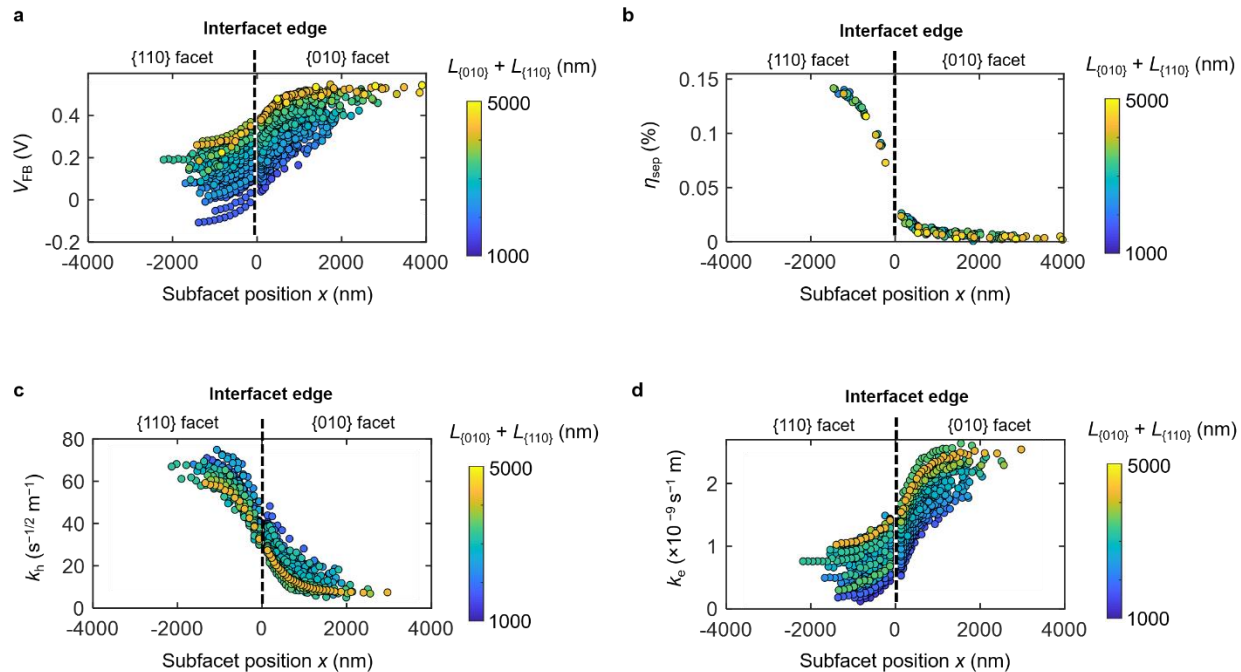


Fig. S15 Subfacet position-dependences of intrinsic materials property parameters: (a) flat-band potential (V_{FB}) (for details, see Supplementary Note 1.3 and 1.7), (b) electron-hole separation efficiency in the SEI depletion zone (η_{sep}) (for details, see Supplementary Note 1.3), (c) effective rate constants k_h that reflects surface hole activities (for details, see Supplementary Note 1.7), and (d) effective rate constants k_e that reflects surface electron activities (for details, see Supplementary Note 1.7). Each color represents one particle. Every circle of the same color indicates a subfacet location on the same particle, determined by either the centroid of a focused probe 405-nm laser (Supplementary Note 1.1) or the location of a dissected segment (Supplementary Note 1.6). Color coding is based on the magnitude of the overall particle size parameter: $L_{\{010\}} + L_{\{110\}}$.

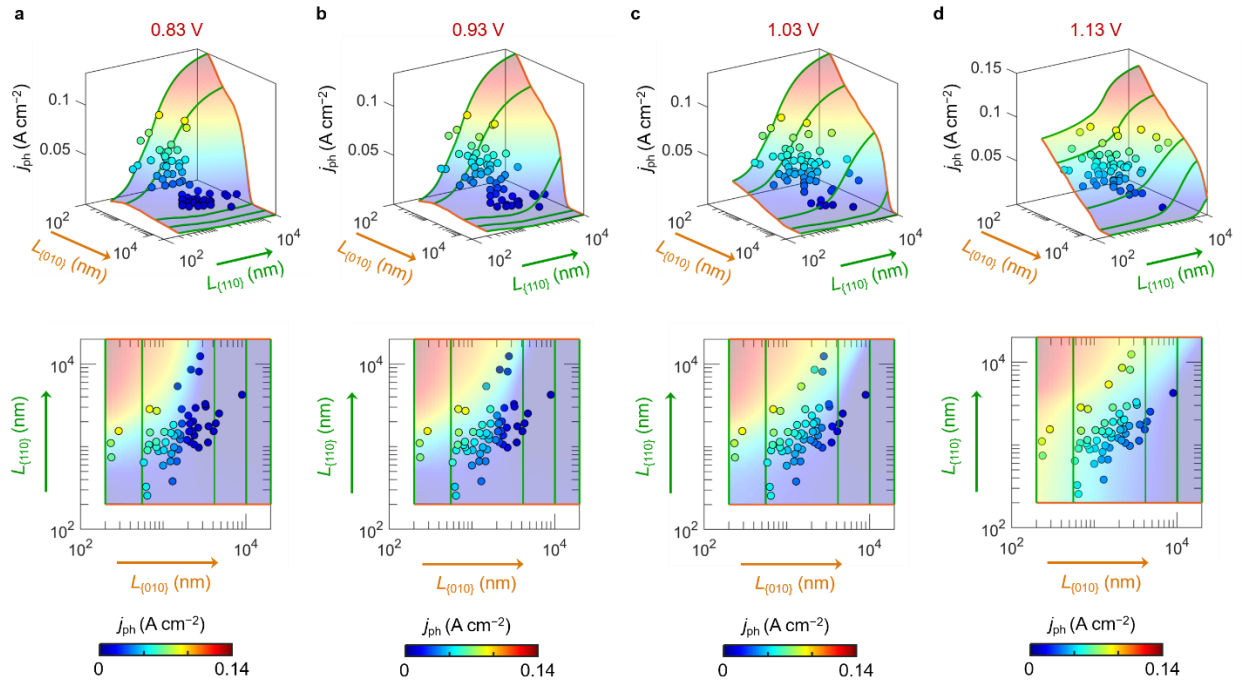


Fig. S16 Single-whole-particle photocurrent densities versus ($L_{\{010\}}$, $L_{\{110\}}$) for as-synthesized BiVO_4 particles at four different potentials: (a) 0.83 V, (b) 0.93 V, (c) 1.03 V, and (d) 1.13 V in a 3D view (upper panels), and in a projected 2D view (lower panels). Circles: experimentally determined single-whole-particle photocurrent densities (for details, see Methods and Supplementary Note 1.9). Shaded surfaces: quantitatively predicted two-dimensional ($L_{\{010\}}$, $L_{\{110\}}$) dependences of single-whole-particle photocurrent densities based on subfacet position-dependent V_{FB} and η_{sep} (for details, see Supplementary Note 2.7). Data presented in d are the same as those in main text Fig. 2e.

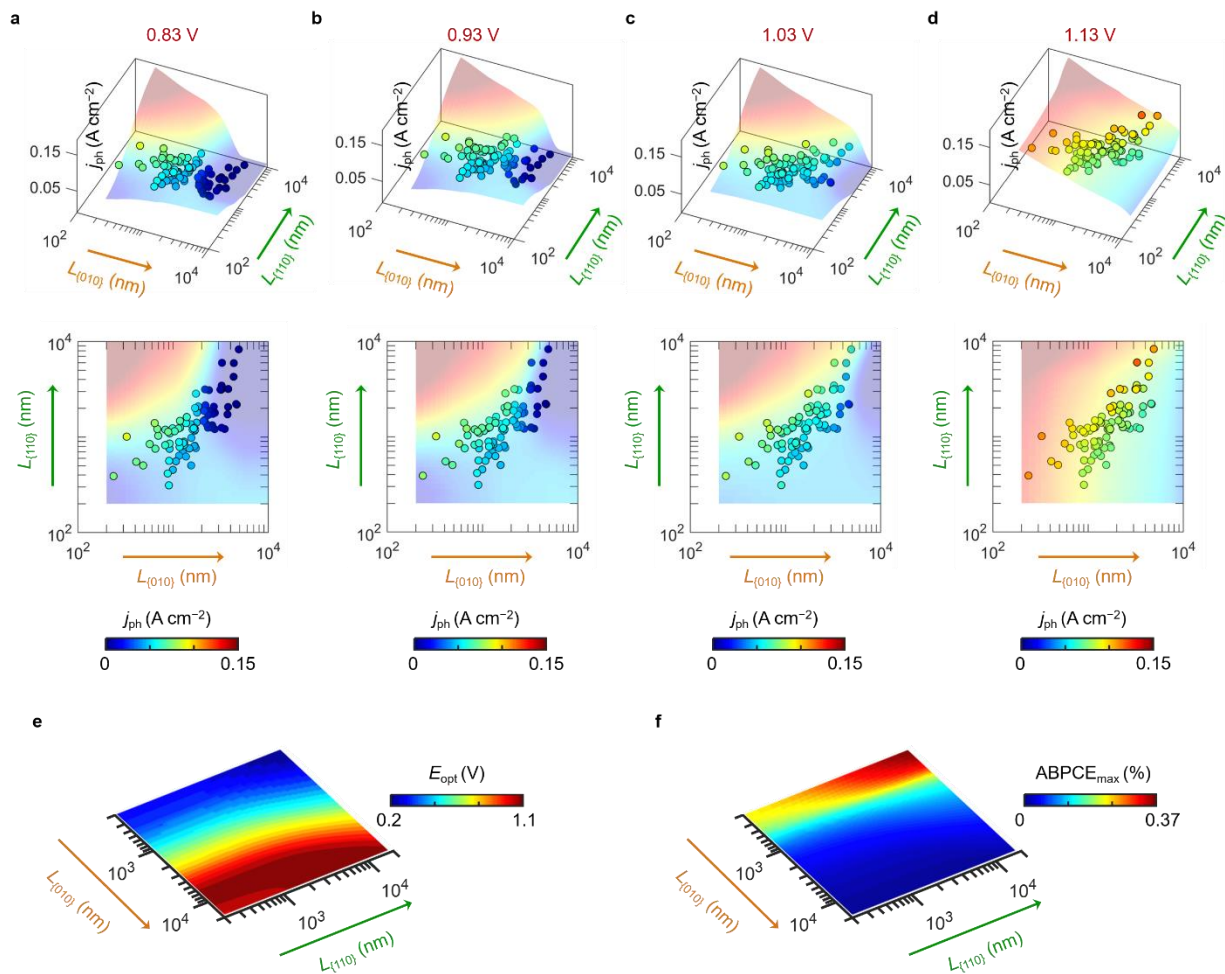


Fig. S17 ($L_{(010)}$, $L_{(110)}$) dependences of single-whole-particle photocurrent densities (j_{ph}), maximally achievable applied-bias photon-to-current efficiency ($ABPCE_{max}$) and corresponding applied potential (E_{opt}) for N_2 -treated $BiVO_4$ particles. (a – d) j_{ph} obtained at four different potentials: 0.83 V (a), 0.93 V (b), 1.03 V (c), and 1.13 V (d) in a 3D view (upper panels), and in a projected 2D view (lower panels). Circles: experimentally determined single-whole-particle photocurrent densities (for details, see Methods and Supplementary Note 1.9). Shaded surfaces: quantitatively predicted two-dimensional ($L_{(010)}$, $L_{(110)}$) dependences of single-whole-particle photocurrent densities based on subfacet position-dependent V_{FB} and η_{sep} (for details, see Supplementary Note 2.7). (e, f) Quantitatively predicted two-dimensional ($L_{(010)}$, $L_{(110)}$) dependences of E_{opt} and $ABPCE_{max}$ (for details, see Supplementary Note 2.8).

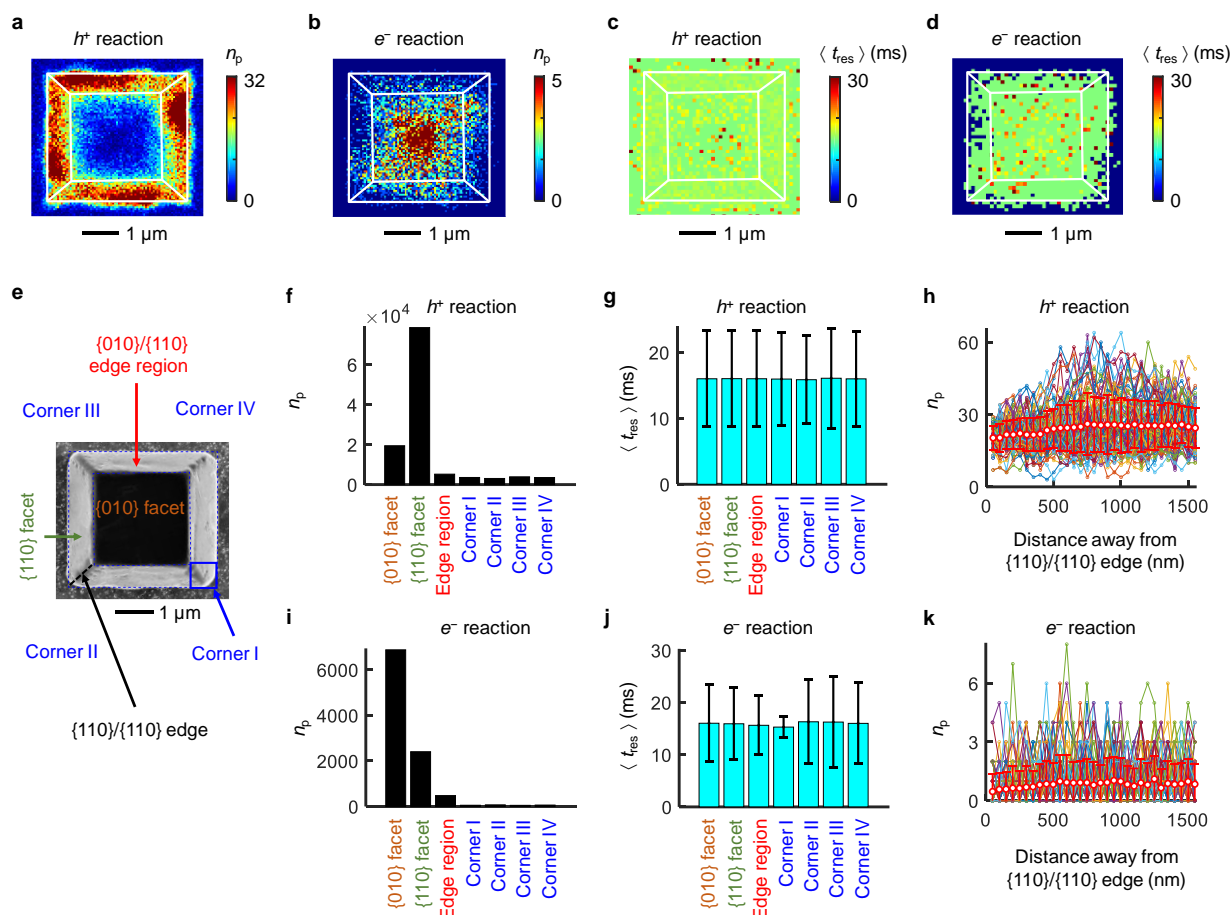


Fig. S18 Analysis of single-molecule fluorescence reaction imaging results of N₂-treated BiVO₄ particles. (a, b) Super-resolution images of h^+ (potential ≥ 0.73 V) (a) and e^- (potential ≤ 0.73 V) (b) induced reactions on the N₂-treated BiVO₄ particle in e. n_p : number of detected product molecules. Bin size: 50.1^2 nm². White lines: structural contours from SEM (e). Imaging duration (each potential): 2.5 min. (c, d) The spatial distribution of the average product molecule residence time ($\langle t_{res} \rangle$) on the N₂-treated BiVO₄ particle in e for the hole-probe reaction (potential ≥ 0.73 V) (c) and the electron-probe reaction (potential ≤ 0.73 V) (d). Bin size: 100.2^2 nm². (e) SEM image of a representative N₂-treated BiVO₄ particle, with illustrations of the lateral {110} facet (orange), the basal {010} facet (green), the {010}/{110} edge region (red), the four corner regions (blue), and the {110}/{110} edge (black) for analyzing the n_p images (a, b) and the $\langle t_{res} \rangle$ images (c, d) to generate the results in f-k. Blue dashed lines indicate the particle structural contour. (f-g) Number of detected product molecules (f) and the averaged value of t_{res} (g) within each subparticle regions defined in e for the hole-probe reaction. Error bars in f and g: s.d. (h) Hole-probe reaction n_p distribution as a function of the distance away from the {110}/{110} edge calculated from the super-resolution h^+ reaction image in a. Each colored dot represents one 50.1^2 nm² pixel in the super-resolution reaction image. Different colors indicate different horizontal or vertical line profiles away from the {110}/{110} edge, similarly as in Fig. S12a. Red circles indicate averages over all the colored line profiles. Error bar: s.d. For calculation details, see Fig. S12a. (i-k) Same as f-h, but for the electron-probe reaction.

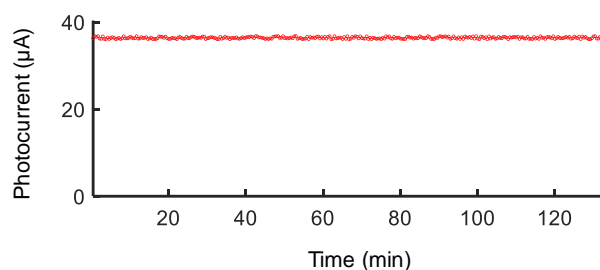


Fig. S19 Photocurrents as a function time measured using a nitrogen-doped BiVO₄ bulk film with an applied potential of 1.13 V in 0.1 M Na₂SO₄, 0.1 M pH 7.4 phosphate buffer. Photocurrents are measured every 25 s with a chopping 405-nm laser of a power density of 12.4 mW/cm².

4 Additional references

- 1 Reichman, J. The current - voltage characteristics of semiconductor - electrolyte junction photovoltaic cells. *Appl. Phys. Lett.* **36**, 574-577 (1980).
- 2 Cendula, P. *et al.* Calculation of the Energy Band Diagram of a Photoelectrochemical Water Splitting Cell. *The Journal of Physical Chemistry C* **118**, 29599-29607 (2014).
- 3 Gärtner, W. W. Depletion-Layer Photoeffects in Semiconductors. *Physical Review* **116**, 84-87 (1959).
- 4 Ma, Y., Pendlebury, S. R., Reynal, A., Le Formal, F. & Durrant, J. R. Dynamics of photogenerated holes in undoped BiVO₄ photoanodes for solar water oxidation. *Chem. Sci.* **5**, 2964-2973 (2014).
- 5 Zhao, Z., Li, Z. & Zou, Z. Electronic structure and optical properties of monoclinic clinobisvanite BiVO₄. *PCCP* **13**, 4746-4753 (2011).
- 6 Sivula, K. & van de Krol, R. Semiconducting materials for photoelectrochemical energy conversion. *Nature Reviews Materials* **1**, 15010 (2016).
- 7 Abdi, F. F., Savenije, T. J., May, M. M., Dam, B. & van de Krol, R. The Origin of Slow Carrier Transport in BiVO₄ Thin Film Photoanodes: A Time-Resolved Microwave Conductivity Study. *J. Phys. Chem. Lett.* **4**, 2752-2757 (2013).
- 8 Rastgar, S. & Wittstock, G. Characterization of Photoactivity of Nanostructured BiVO₄ at Polarized Liquid-Liquid Interfaces by Scanning Electrochemical Microscopy. *The Journal of Physical Chemistry C* **121**, 25941-25948 (2017).
- 9 Alderman, N., Ibrahim, M. A., Danos, L., Grossel, M. C. & Markvart, T. Determination of surface recombination velocities of organic monolayers on silicon through Kelvin probe. *Appl. Phys. Lett.* **103**, 081603 (2013).
- 10 Zachäus, C., Abdi, F. F., Peter, L. M. & van de Krol, R. Photocurrent of BiVO₄ is limited by surface recombination, not surface catalysis. *Chemical Science* **8**, 3712-3719 (2017).
- 11 Butler, K. T. *et al.* Ultrafast carrier dynamics in BiVO₄ thin film photoanode material: interplay between free carriers, trapped carriers and low-frequency lattice vibrations. *Journal of Materials Chemistry A* **4**, 18516-18523 (2016).

- 12 Sambur, J. B. *et al.* Sub-particle reaction and photocurrent mapping to optimize catalyst-modified photoanodes. *Nature* **530**, 77-80 (2016).
- 13 Mao, X., Liu, C., Hesari, M., Zou, N. & Chen, P. Super-resolution imaging of non-fluorescent reactions via competition. *Nat Chem* **11**, 687-694 (2019).
- 14 Chen, T. Y. *et al.* Concentration- and chromosome-organization-dependent regulator unbinding from DNA for transcription regulation in living cells. *Nat. Commun.* **6**, 7445 (2015).
- 15 Chen, P. & Chen, T.-Y. *MATLAB code package: iQPALM (image-based quantitative photo-activated localization microscopy)*. DOI: 10.6084/m9.figshare.12642617.v1. (2020).
- 16 Sambur, J. B. *et al.* Sub-particle reaction and photocurrent mapping to optimize catalyst-modified photoanodes. *Nature* **530**, 77 (2016).
- 17 Sambur, J. B. *et al.* Correlated Single-Molecule Reaction Imaging and Photocurrent Measurements Reveal Underlying Rate Processes in Photoelectrochemical Water Splitting. *J. Electrochem. Soc.* **166**, H3286-H3293 (2019).
- 18 Xu, W., Jain, P. K., Beberwyck, B. J. & Alivisatos, A. P. Probing Redox Photocatalysis of Trapped Electrons and Holes on Single Sb-doped Titania Nanorod Surfaces. *J. Am. Chem. Soc.* **134**, 3946-3949 (2012).
- 19 Zhang, Y. *et al.* Superresolution fluorescence mapping of single-nanoparticle catalysts reveals spatiotemporal variations in surface reactivity. *Proceedings of the National Academy of Sciences* **112**, 8959-8964 (2015).
- 20 Shen, H., Zhou, X., Zou, N. & Chen, P. Single-Molecule Kinetics Reveals a Hidden Surface Reaction Intermediate in Single-Nanoparticle Catalysis. *The Journal of Physical Chemistry C* **118**, 26902-26911 (2014).
- 21 Reichman, J. Collection efficiency of low-mobility solar cells. *Appl. Phys. Lett.* **38**, 251-253 (1981).
- 22 Parmon, V. N. Thermodynamic analysis of the effect of the nanoparticle size of the active component on the adsorption equilibrium and the rate of heterogeneous catalytic processes. *Dokl Phys Chem* **413**, 42-48 (2007).
- 23 Zhou, X. C., Xu, W. L., Liu, G. K., Panda, D. & Chen, P. Size-Dependent Catalytic Activity and Dynamics of Gold Nanoparticles at the Single-Molecule Level. *J. Am. Chem. Soc.* **132**, 138-146 (2010).
- 24 Yudanov, I. V., Genest, A., Schauermaun, S., Freund, H. J. & Rosch, N. Size Dependence of the Adsorption Energy of CO on Metal Nanoparticles: A DFT Search for the Minimum Value. *Nano Lett.* **12**, 2134-2139 (2012).
- 25 Ye, K.-H. *et al.* Enhancing photoelectrochemical water splitting by combining work function tuning and heterojunction engineering. *Nat Commun* **10**, 3687 (2019).
- 26 Nipane, A., Jayanti, S., Borah, A. & Teherani, J. T. Electrostatics of lateral p-n junctions in atomically thin materials. *J. Appl. Phys.* **122**, 194501 (2017).
- 27 Kim, T. W., Ping, Y., Galli, G. A. & Choi, K.-S. Simultaneous enhancements in photon absorption and charge transport of bismuth vanadate photoanodes for solar water splitting. *Nat Commun* **6**, 8769 (2015).
- 28 Baroni, S., de Gironcoli, S., Dal Corso, A. & Giannozzi, P. Phonons and related crystal properties from density-functional perturbation theory. *Reviews of Modern Physics* **73**, 515-562 (2001).

- 29 Rettie, A. J. E. *et al.* Combined Charge Carrier Transport and Photoelectrochemical Characterization of BiVO₄ Single Crystals: Intrinsic Behavior of a Complex Metal Oxide. *J. Am. Chem. Soc.* **135**, 11389-11396 (2013).
- 30 Austin, I. G. & Mott, N. F. Polarons in crystalline and non-crystalline materials. *Advances in Physics* **18**, 41-102 (1969).
- 31 Yang, J., Wang, D., Zhou, X. & Li, C. A Theoretical Study on the Mechanism of Photocatalytic Oxygen Evolution on BiVO₄ in Aqueous Solution. *Chemistry – A European Journal* **19**, 1320-1326 (2013).
- 32 Kim, T. W. & Choi, K.-S. Nanoporous BiVO₄ Photoanodes with Dual-Layer Oxygen Evolution Catalysts for Solar Water Splitting. *Science* **343**, 990-994 (2014).
- 33 Li, R. G. *et al.* Spatial separation of photogenerated electrons and holes among {010} and {110} crystal facets of BiVO₄. *Nat. Commun.* **4**, 1432 (2013).
- 34 Park, Y., McDonald, K. J. & Choi, K.-S. Progress in bismuth vanadate photoanodes for use in solar water oxidation. *Chem. Soc. Rev.* **42**, 2321-2337 (2013).
- 35 Nellist, M. R., Laskowski, F. A. L., Lin, F., Mills, T. J. & Boettcher, S. W. Semiconductor–Electrocatalyst Interfaces: Theory, Experiment, and Applications in Photoelectrochemical Water Splitting. *Acc. Chem. Res.* **49**, 733-740 (2016).
- 36 Walter, M. G. *et al.* Solar Water Splitting Cells. *Chem. Rev.* **110**, 6446-6473 (2010).
- 37 Ma, Y., Kafizas, A., Pendlebury, S. R., Le Formal, F. & Durrant, J. R. Photoinduced Absorption Spectroscopy of CoPi on BiVO₄: The Function of CoPi during Water Oxidation. *Adv. Funct. Mater.* **26**, 4951-4960 (2016).
- 38 Ma, Y., Le Formal, F., Kafizas, A., Pendlebury, S. R. & Durrant, J. R. Efficient suppression of back electron/hole recombination in cobalt phosphate surface-modified undoped bismuth vanadate photoanodes. *Journal of Materials Chemistry A* **3**, 20649-20657 (2015).
- 39 Klahr, B., Gimenez, S., Fabregat-Santiago, F., Bisquert, J. & Hamann, T. W. Photoelectrochemical and Impedance Spectroscopic Investigation of Water Oxidation with “Co–Pi”-Coated Hematite Electrodes. *J. Am. Chem. Soc.* **134**, 16693-16700 (2012).
- 40 Carroll, G. M., Zhong, D. K. & Gamelin, D. R. Mechanistic insights into solar water oxidation by cobalt-phosphate-modified α -Fe₂O₃ photoanodes. *Energy & Environmental Science* **8**, 577-584 (2015).
- 41 Carroll, G. M. & Gamelin, D. R. Kinetic analysis of photoelectrochemical water oxidation by mesostructured Co-Pi/ α -Fe₂O₃ photoanodes. *Journal of Materials Chemistry A* **4**, 2986-2994 (2016).
- 42 Barroso, M. *et al.* The Role of Cobalt Phosphate in Enhancing the Photocatalytic Activity of α -Fe₂O₃ toward Water Oxidation. *J. Am. Chem. Soc.* **133**, 14868-14871 (2011).
- 43 Barroso, M. *et al.* Dynamics of photogenerated holes in surface modified α -Fe₂O₃ photoanodes for solar water splitting. *Proceedings of the National Academy of Sciences* **109**, 15640-15645 (2012).
- 44 Zhu, J. *et al.* Visualizing the Nano Cocatalyst Aligned Electric Fields on Single Photocatalyst Particles. *Nano Lett.* **17**, 6735-6741 (2017).
- 45 Chen, R. *et al.* Charge separation via asymmetric illumination in photocatalytic Cu₂O particles. *Nature Energy* **3**, 655-663 (2018).

- 46 Nellist, M. R. *et al.* Potential-sensing electrochemical atomic force microscopy for in operando analysis of water-splitting catalysts and interfaces. *Nature Energy* **3**, 46-52 (2018).
- 47 Martin, D. J., Umezawa, N., Chen, X., Ye, J. & Tang, J. Facet engineered Ag₃PO₄ for efficient water photooxidation. *Energy & Environmental Science* **6**, 3380-3386 (2013).
- 48 Li, D. *et al.* Crystallographic-Orientation-Dependent Charge Separation of BiVO₄ for Solar Water Oxidation. *ACS Energy Letters* **4**, 825-831 (2019).
- 49 Takata, T. *et al.* Photocatalytic water splitting with a quantum efficiency of almost unity. *Nature* **581**, 411-414 (2020).
- 50 Chen, S., Takata, T. & Domen, K. Particulate photocatalysts for overall water splitting. *Nature Reviews Materials* **2**, 17050 (2017).
- 51 Liu, G., Yu, J. C., Lu, G. Q. & Cheng, H.-M. Crystal facet engineering of semiconductor photocatalysts: motivations, advances and unique properties. *Chem. Commun.* **47**, 6763-6783 (2011).
- 52 Xie, Y. P., Liu, G., Yin, L. & Cheng, H.-M. Crystal facet-dependent photocatalytic oxidation and reduction reactivity of monoclinic WO₃ for solar energy conversion. *J. Mater. Chem.* **22**, 6746-6751 (2012).
- 53 Mu, L. *et al.* Enhancing charge separation on high symmetry SrTiO₃ exposed with anisotropic facets for photocatalytic water splitting. *Energy & Environmental Science* **9**, 2463-2469 (2016).
- 54 Luo, Y. *et al.* Construction of Spatial Charge Separation Facets on BaTaO₂N Crystals by Flux Growth Approach for Visible-Light-Driven H₂ Production. *ACS Applied Materials & Interfaces* **11**, 22264-22271 (2019).
- 55 Ham, Y. *et al.* Flux-mediated doping of SrTiO₃ photocatalysts for efficient overall water splitting. *Journal of Materials Chemistry A* **4**, 3027-3033 (2016).
- 56 Takata, T. & Domen, K. Defect Engineering of Photocatalysts by Doping of Aliovalent Metal Cations for Efficient Water Splitting. *The Journal of Physical Chemistry C* **113**, 19386-19388 (2009).
- 57 Goto, Y. *et al.* A Particulate Photocatalyst Water-Splitting Panel for Large-Scale Solar Hydrogen Generation. *Joule* **2**, 509-520 (2018).
- 58 Maeda, K. & Domen, K. Photocatalytic Water Splitting: Recent Progress and Future Challenges. *The Journal of Physical Chemistry Letters* **1**, 2655-2661 (2010).
- 59 Crespo-Otero, R. & Walsh, A. Variation in Surface Ionization Potentials of Pristine and Hydrated BiVO₄. *The Journal of Physical Chemistry Letters* **6**, 2379-2383 (2015).
- 60 Lardhi, S., Cavallo, L. & Harb, M. Significant Impact of Exposed Facets on the BiVO₄ Material Performance for Photocatalytic Water Splitting Reactions. *The Journal of Physical Chemistry Letters*, 5497-5503 (2020).